EUROfusion

WPMAT

Nano-cluster defects in W&W alloys: Uncertainty quantification assessment from multi-scale modelling

Duc Nguyen-Manh

Culham Centre of Fusion Energy, UKAEA

Supported by EuroFusion, FP7 and IFERC-CSC projects

Collaborators: F. Hofmann, D. Mason, J. Wrobel, S. Dudarev

IAEA Technical Meeting CCN4, Vienna, 29-31 July 2015

Energy

CCFE is the fusion research arm of the **United Kingdom Atomic Energy Authority.**
This work was funded by the RCUK Energy Programme [grant number EP/I501045] .

CCFE
CULHAM CENTRE FOR FUSION ENERGY

EUROfusion

WPMAT

Multi-scale materials modelling

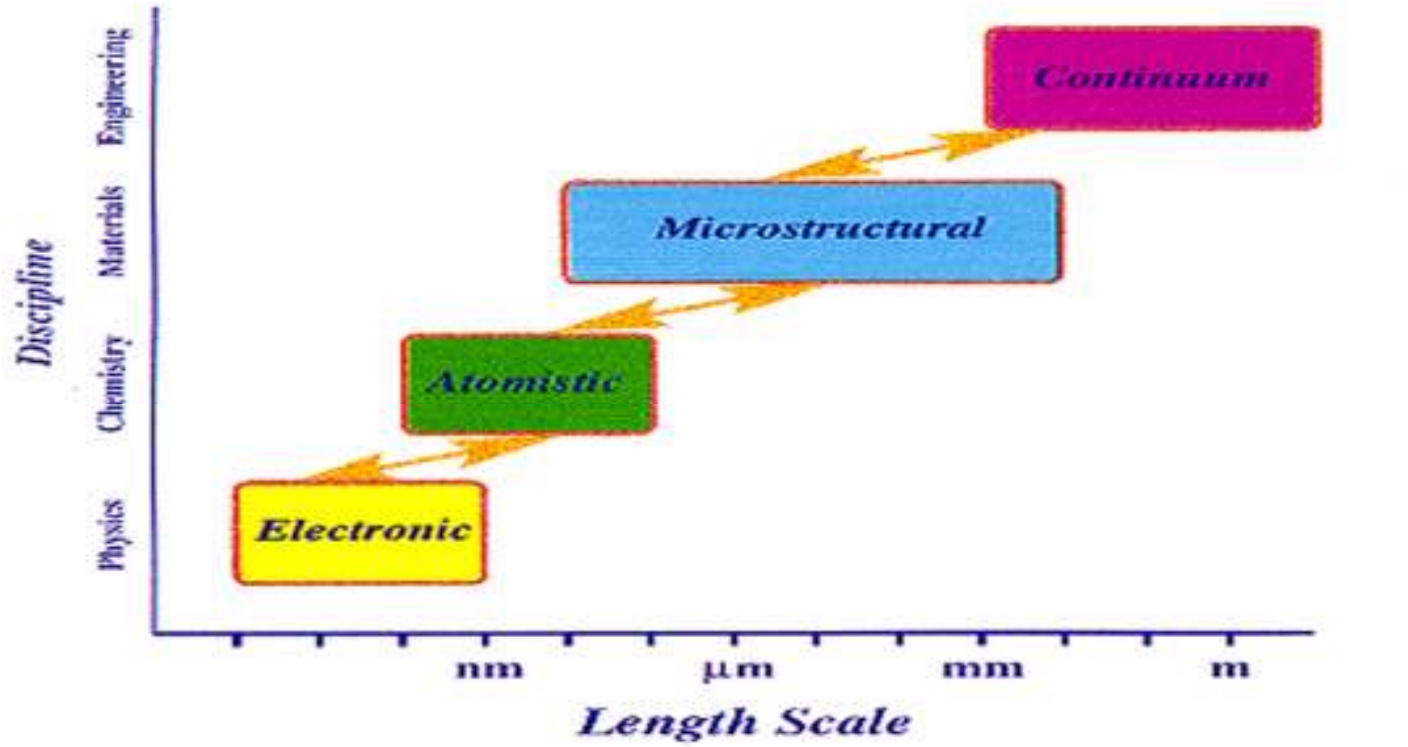

Hierarchy of Models in Materials Research

DNM, Bratkovsky, Pettifor, Phil. Trans. Roy. Soc. Lond. ,315 (1995) 529

EUROfusion

WPMAT

DFT -> Interatomic potentials -> plastic deformation

REPORTS

Origin of Brittle Cleavage in Iridium

Marc J. Cawkwell,[1*] Duc Nguyen-Manh,[2] Christopher Woodward,[3,4] David G. Pettifor,[5] Vaclav Vitek[1]

Iridium is unique among the face-centered cubic metals in that it undergoes brittle cleavage after a period of plastic deformation under tensile stress. Atomistic simulation using a quantum-mechanically derived bond-order potential shows that in iridium, two core structures for the screw dislocation are possible: a glissile planar core and a metastable nonplanar core. Transformation between the two core structures is athermal and leads to exceptionally high rates of cross slip during plastic deformation. Associated with this athermal cross slip is an exponential increase in the dislocation density and strong work hardening from which brittle cleavage is a natural consequence.

The plastic deformation of crystalline materials is mediated by the motion of line defects called dislocations (*1*). Dislocations glide along crystallographic planes and displace the two parts of the crystal by a fixed lattice vector known as the Burgers vector. If metastable stacking faults can form, dislocations may reduce their energy by dissociating into partials with Burgers vectors smaller than the lattice vector, connected by the stacking fault. The equilibrium width of splitting is determined by a balance of elastic repulsion between the partials and attraction arising from the energy of the stacking fault. The mobility of individual dislocations is to a large extent governed by the shape of their cores. Dislocations with cores that are spread only on the slip plane are hereafter referred to as planar and are usually glissile; i.e., they move easily at very low applied stresses even at low temperatures. Dislocations with cores that are spread onto two or more nonparallel planes are hereafter referred to as nonplanar and tend to be sessile; i.e., in order to glide, they require high stresses that are often strongly dependent on temperature

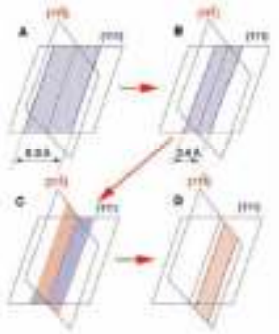

Fig. 3. Schematic diagram of athermal cross slip in iridium. (A and B) The splitting between Shockley partials is constricted from 8.0 to about 3.4 Å, where the dislocations with the planar and nonplanar cores become energetically equivalent. (C) Long segments of the nonplanar core spontaneously form along the screw dislocation line. (D) The nonplanar core transforms under the effect of glide and Escaig stress into Shockley partials on the cross-slip plane.

Fig. 2. Energy of screw dislocation with planar and nonplanar cores. The dashed line shows the energy of the dislocation dissociated into Shockley partials constricted by an Escaig stress of 0.0250 C_{44}

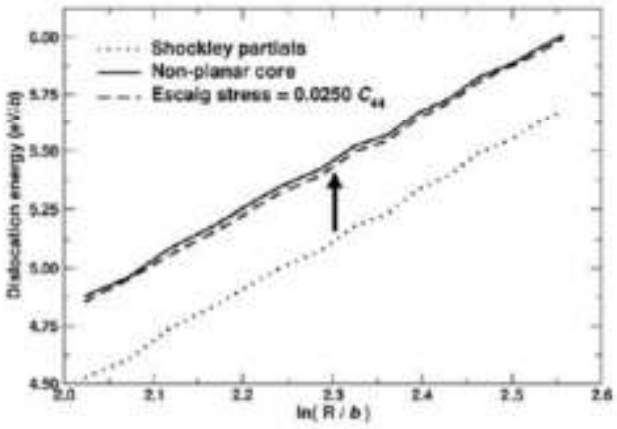

EUROfusion

WPMAT

Microstructures in irradiated materials

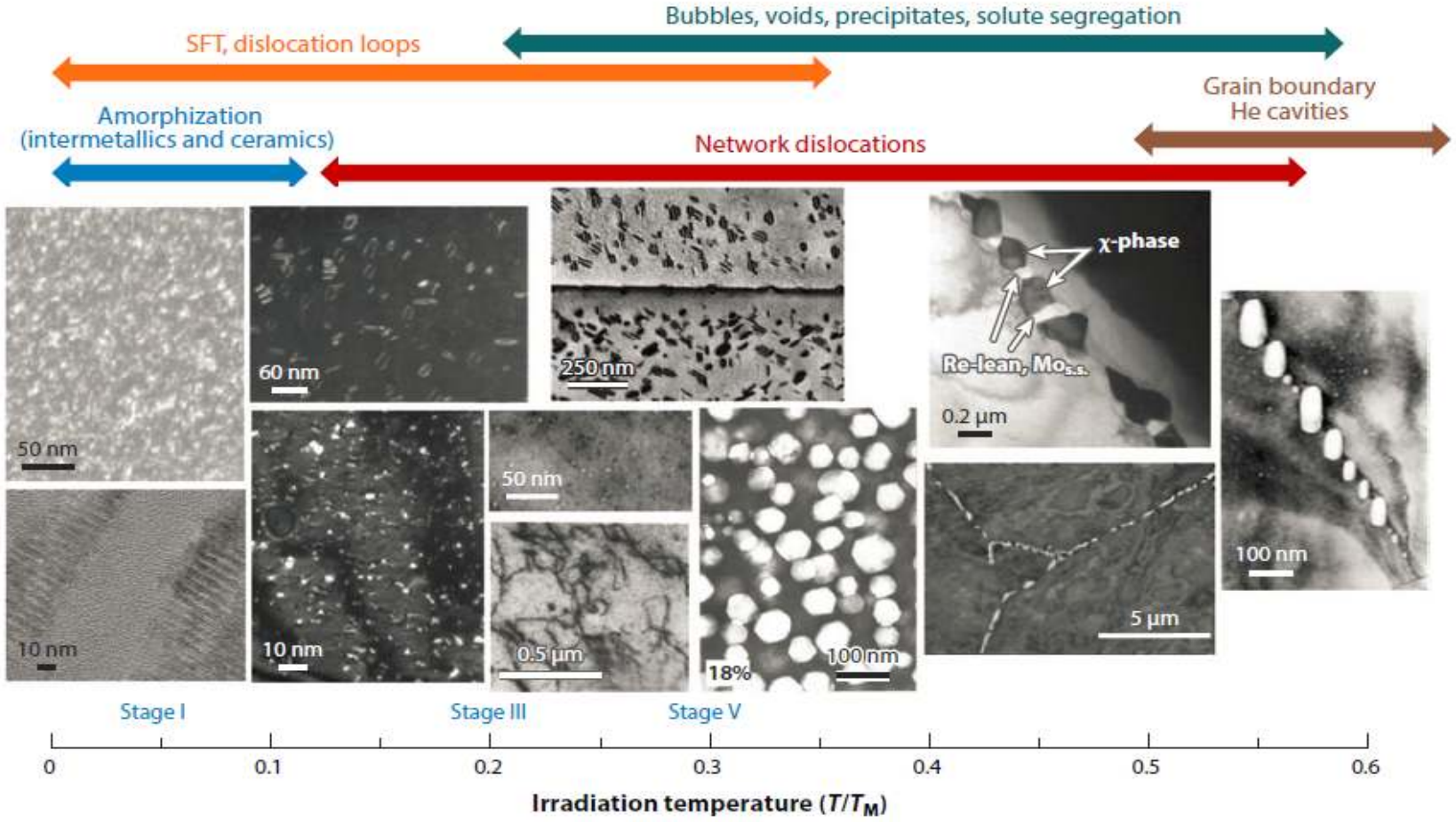

S.J, Zinkle and L.L. Snead, Annu. Rev. Mater. Res. , 44, 241 (2014)

EUROfusion

WPMAT

Transmutation effect under neutron irradiation

- 5 fpy irradiation of pure W in most exposed region of the divertor armour (hcpb – total flux of 5.5×10^{14} n cm^{-2} s^{-1})

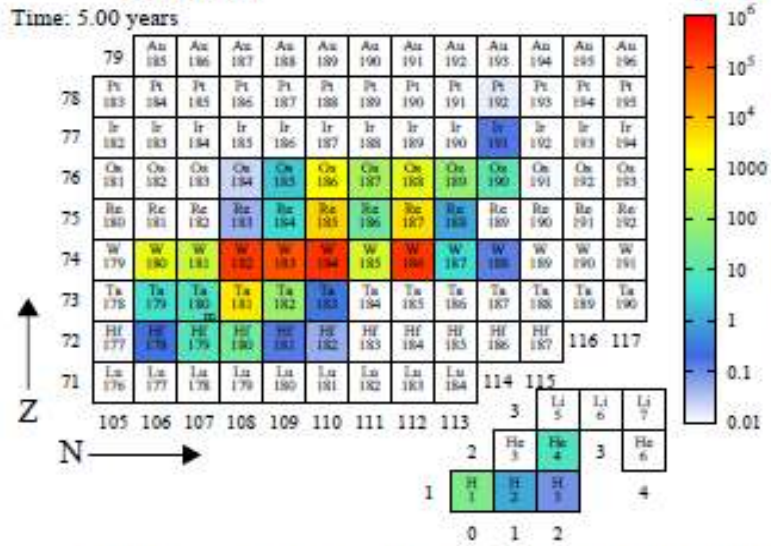

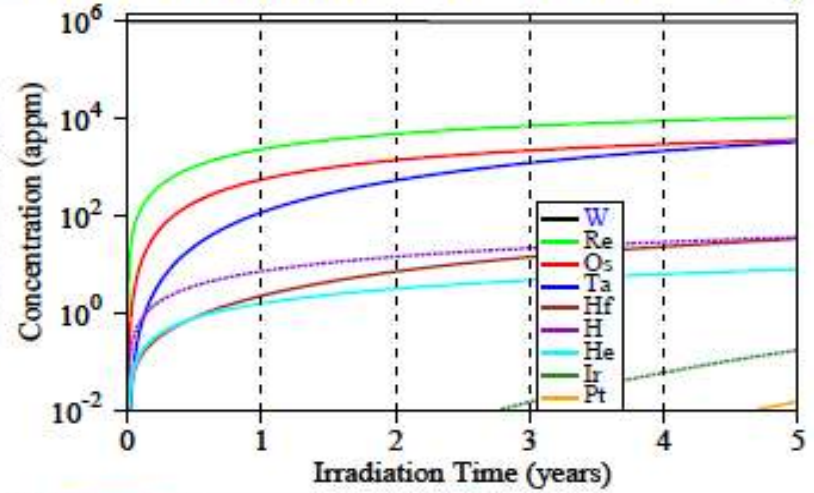

- After 5 fpy, the originally 100% W contains 1% Re, 0.4% Ta, 0.3% Os and smaller amounts of Hf, Ir, Pt, H and He

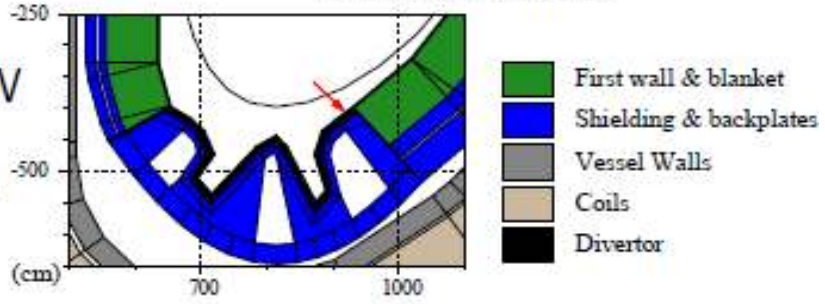

EUROfusion

WPMAT

Integrated modelling of fusion power-plant
Systematic ab-initio data base of defect energetics

Using the available *ab-initio* modelling methods for modelling the degree of de-cohesion at grain boundaries due to helium accumulation, and combining it with neutron transport and transmutation rate analysis for evaluating the rate of helium accumulation in an integrated multi-scale study of neutron-induced dpa, transmutations, gas production, helium embrittlement of fusion materials.

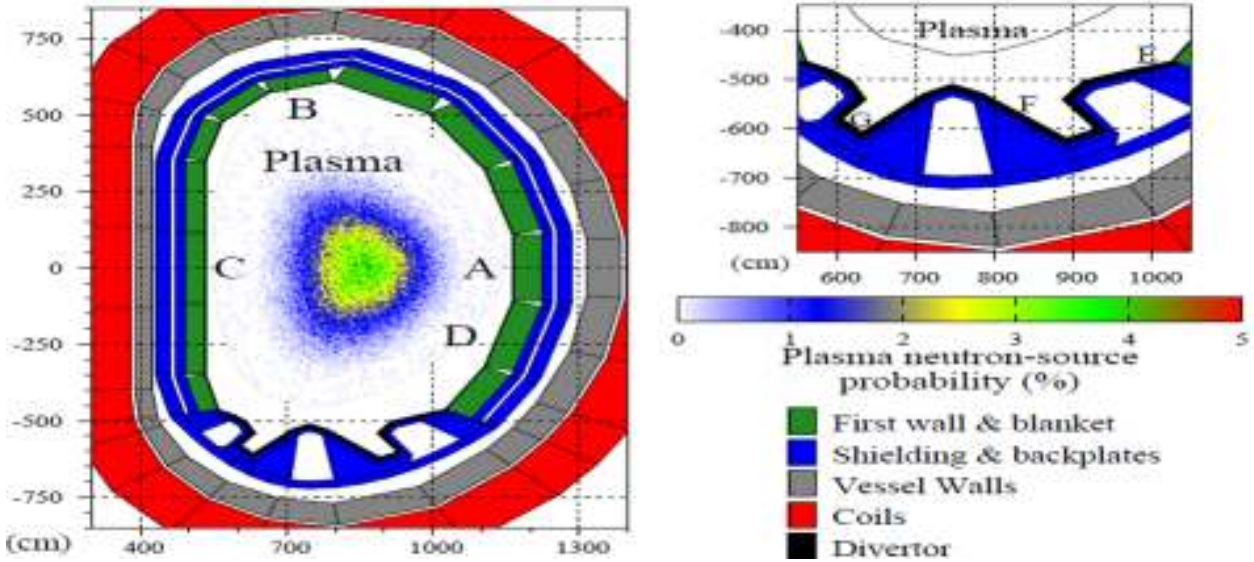

M.R. Gilbert, S.L. Dudarev, DNM, S. Zheng, L.W. Packer, J.C. Sublet JNM 442 (2013), S755-S760

CCFE CULHAM CENTRE FOR FUSION ENERGY

EUROfusion

WPMAT

OUTLINE

- Systematic assessment from electronic level
- He clusters trapping by noble-gas impurities in W vs. TDS measurements
- Lattice swelling & modulus changes in irradiated W: XRMD & SAW vs. MM
- Nano-clusters of vacancies vs. TEM of high-temperature annealing irradiated W
- Anomalous precipitation in self-ion irradiated W-Re alloys vs. APT experiments

EUROfusion

WPMAT

Integrated view of materials in DEMO fusion

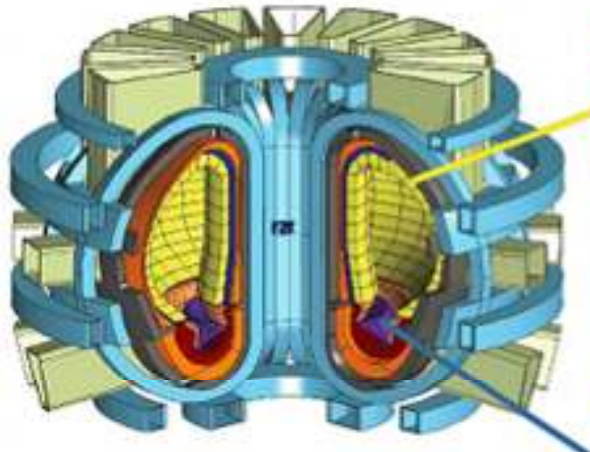

Power plant 0

An exceedingly challenging materials science and engineering problem.

M. Rieth, 2011

Blanket: ≤150 dpa/5 years, 2.5 MW/m²

Reduced activation ferritic-c steels, assuming

→ EUROFER (9Cr-WVTa) 350-550 °C
→ ODS-EUROFER 350-650 °C

He cooled structure, liquid lithium or lithium-ceramics for tritium breeding; ~85 % power

Divertor: ~30 dpa/2 years, ≥10MW/m²

Materials, cooling method: undecided
Operating temperature 350-1300 °C ?

Cooled tungsten shield to sustain direct impact of He and other particles from plasma, absorbing ~15% of total fusion power

Divertor's function is to extract heat, He ash and impurities from plasma

CCFE CULHAM CENTRE FOR FUSION ENERGY

EUROfusion

WPMAT

Electronic level: challenge with bcc TMs & alloys

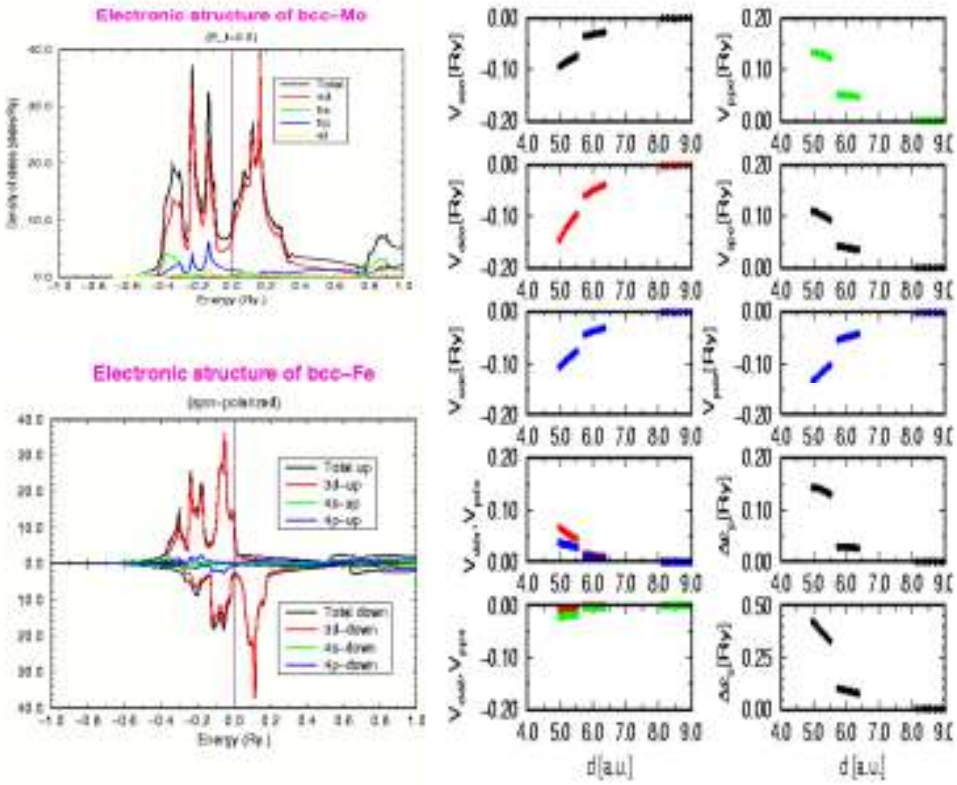

DNM, D.G. Pettifor, V. Vitek, PRL, 85, 4136 (2000)

ELSEVIER

Available online at www.sciencedirect.com
ScienceDirect
Progress in Materials Science 52 (2007) 255–298

Progress in Materials Science
www.elsevier.com/locate/pmatsci

Environmental dependence of bonding: A challenge for modelling of intermetallics and fusion materials

D. Nguyen-Manh [a,*], V. Vitek [b], A.P. Horsfield [c]

[a] EURATOM/UKAEA Fusion Association, Culham Science Centre, Abingdon, Oxford OX14 3DB, UK
[b] Department of Materials Science and Engineering, University of Pennsylvania, Philadelphia, PA 19104-6257, USA
[c] Department of Physics and Astronomy, University College London, London WC1E 6BT, UK

Abstract

Bridging the gap between electronic and atomistic levels plays a crucial role in multi-scale modelling of mechanical behaviour of materials. In this review, we summarise a methodology for linking systematically these two levels starting from the first-principles density functional theory and proceeding via the screened tight-binding approximation to development of reliable and transferable many-body interatomic bond-order potentials. We focus our investigations on material properties related to the electron-to-atom ratio. An immediate area of application is studies of the structure and properties of crystal defects in transition metals and intermetallic compounds based on transition metals, where the mixed character of covalent and metallic bonds represents a very challenging issue for understanding mechanical properties at the engineering scale. The need for environmental dependence of bond-order potentials as well as the implication of screening effects on bonding properties of alloys are discussed in connection with modelling of the core structure of dislocations in materials with negative Cauchy pressures and in body-centered cubic (bcc) transition metals. The latter are prime candidates as fusion power-plant materials. We discuss our current work on multiscale modelling, the behaviour of bcc materials under high-energy neutron irradiation, and emphasize the importance of quantum-mechanics in constructing reliable interatomic potentials for large scale molecular dynamic simulations.

EUROfusion

WPMAT

Systematic studies of electronic structure (group 5B vs. 6B) effects for radiation damage

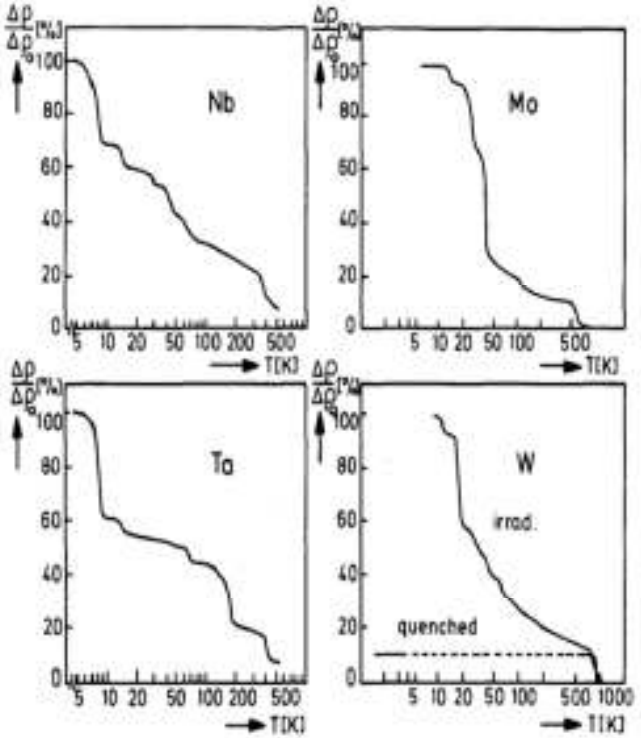

Fig. 4. Recovery curves for several bcc metals. The ratio residual resistivity $\Delta\rho$, observed at low temperature during an isochronal annealing procedure with a step-by-step increased annealing temperature, over the residual resistivity $\Delta\rho_0$ before annealing, is plotted versus the temperature T of the last step. This figure is taken from ref. [1].

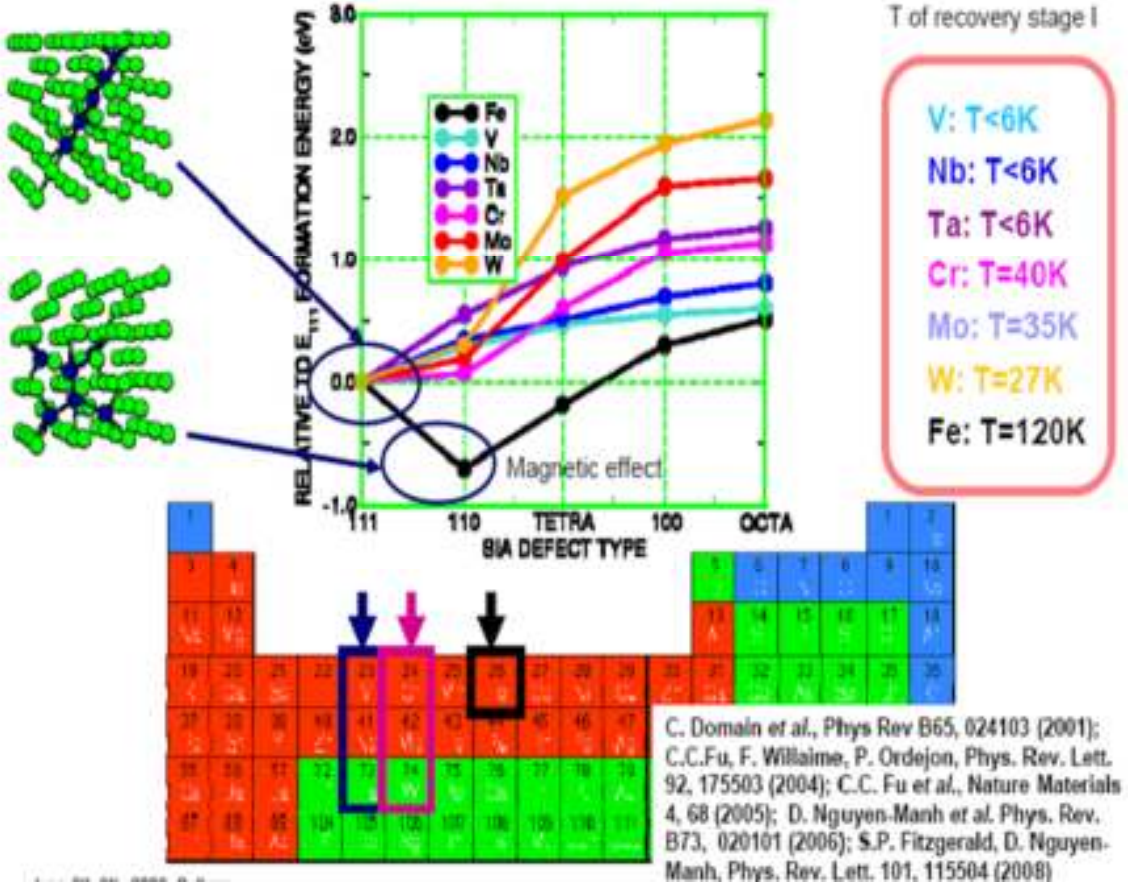

C. Domain *et al.*, Phys Rev B65, 024103 (2001); C.C.Fu, F. Willaime, P. Ordejon, Phys. Rev. Lett. 92, 175503 (2004); C.C. Fu *et al.*, Nature Materials 4, 68 (2005); D. Nguyen-Manh *et al.* Phys. Rev. B73, 020101 (2006); S.P. Fitzgerald, D. Nguyen-Manh, Phys. Rev. Lett. 101, 115504 (2008)

Crowdion motion: Frenkel-Kontorova model

$$\mathcal{L} = \sum_{n=-\infty}^{\infty} \left(\frac{m\dot{u}_n^2}{2} - \frac{\beta}{2}(u_{n+1} - u_n)^2 - V(u_n) \right)$$

"Spring constant" (along string)

Displacement of *n*th atom from position *na*

Periodic potential, period *a*

EUROfusion

WPMAT

Migration barriers of crowdion

- Simple sine potential not good for bcc transition metals
- Double-sine captures double-hump
- Previous analysis carries through with some complications

$$V_0\left(\sin^2\frac{\pi z}{a}+\frac{\alpha^2-1}{4}\sin^2\frac{2\pi z}{a}\right)$$

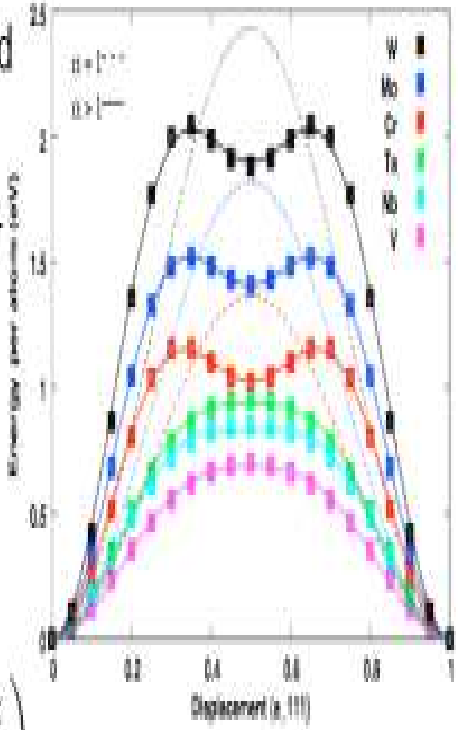

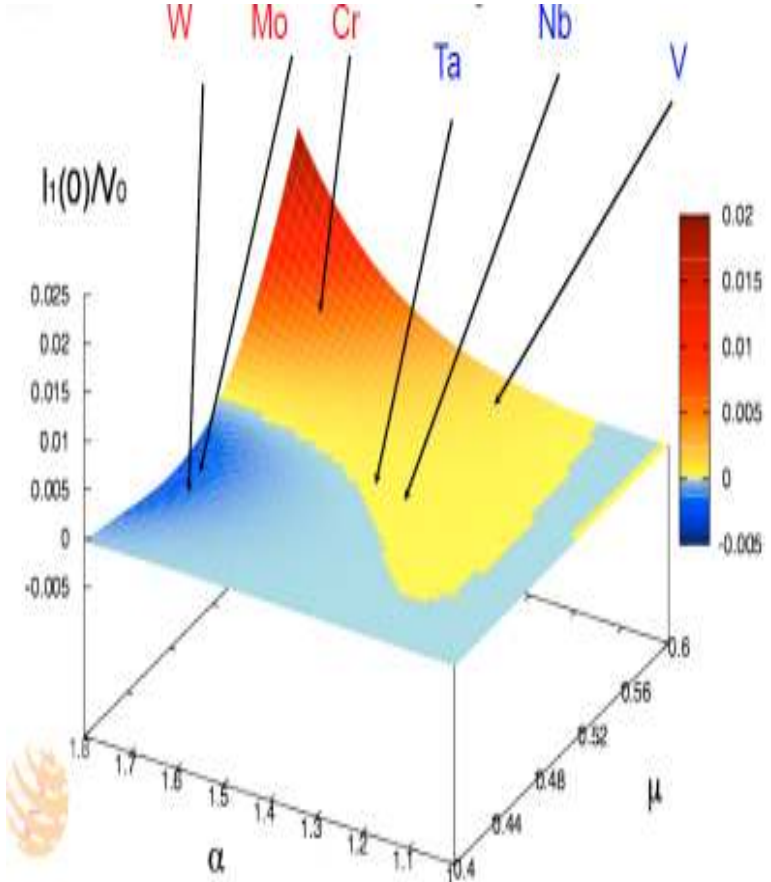

Analytic solutions: S.P. Fitzgerald, DNM, PRL, 101 (2008) 115504

EUROfusion

WPMAT

In situ TEM observation of 1D nanometer-size SIA loops

Observation of the One-Dimensional Diffusion of Nanometer-Sized Dislocation Loops

K. Arakawa,[1]* K. Ono,[2] M. Isshiki,[3] K. Mimura,[3] M. Uchikoshi,[3] H. Mori[1]

Dislocations are ubiquitous linear defects and are responsible for many of the properties of crystalline materials. Studies on the glide process of dislocations in bulk materials have mostly focused on the response of dislocations with macroscopic lengths to external loading or unloading. Using in situ transmission electron microscopy, we show that nanometer-sized loops with a Burgers vector of ½(111) in α-Fe can undergo one-dimensional diffusion even in the absence of stresses that are effective in driving the loops. The loop size dependence of the loop diffusivity obtained is explained by the stochastic thermal fluctuation in the numbers of double kinks.

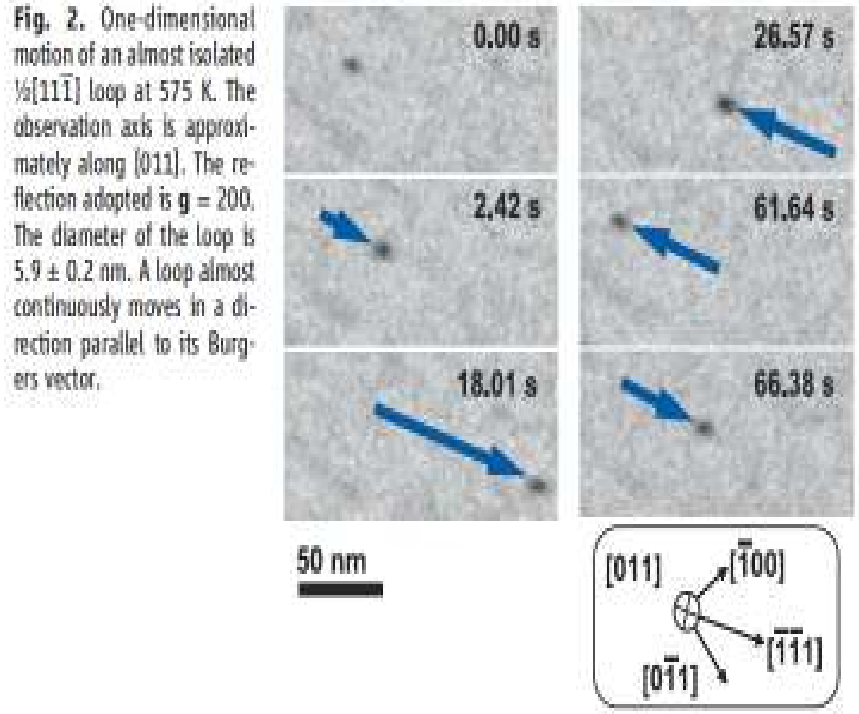

Fig. 2. One-dimensional motion of an almost isolated ½[11$\bar{1}$] loop at 575 K. The observation axis is approximately along [011]. The reflection adopted is **g** = 200. The diameter of the loop is 5.9 ± 0.2 nm. A loop almost continuously moves in a direction parallel to its Burgers vector.

Science, 318, 9th Nov. 2007

EUROfusion

WPMAT

Noble-gas ion implantation to simulate neutron-induced damage

•Fast neutrons lead to the formation of large amount of He and H via the nuclear transmutation reactions giving rise to radiation swelling and grain boundary embrittlement. So far, most of investigation has been focused on He atoms behaviour in the radiation environment of fusion reactor systems

•Multi-beam ion implantation experiments promote new ideas to consider He co-implanting with other inert-gas ions (Ne, Ar, Kr, Xe) to simultaneously get dpa damage and dissolved noble gases. A question arises as to whether inert-gas atoms would be a good analogue for He?

•The effect of inert gases incorporation in bcc transition metals has not been systematically studied even though the agglomeration of noble gas atoms is important in understanding swelling in fission reaction (Xe atoms are is produced in the reaction with uranium and trend to coalesce into bubbles in uranium dioxide). Traditional view is that there is a similarity between He and other inter-gas atoms because of no chemical interactions and only local distortion increases from He to Ne, Ar, Kr, Xe.

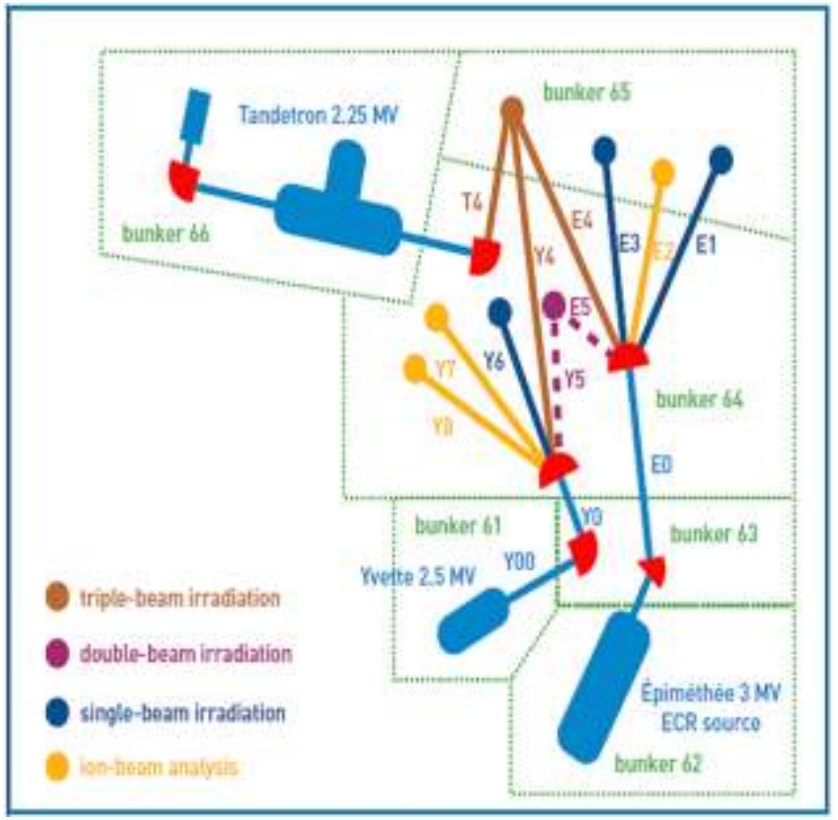

JANNuS platform: Ion-beam simulation of materials science (Y. Serruys et al.)

CCFE
CULHAM CENTRE FOR FUSION ENERGY

EUROfusion

WPMAT

Thermal Desorption Spectra in bcc-W : Interaction of injected He with lattice defects

E.V. Kornelsen, Rad. Effects, vol. 13 (1972) 227

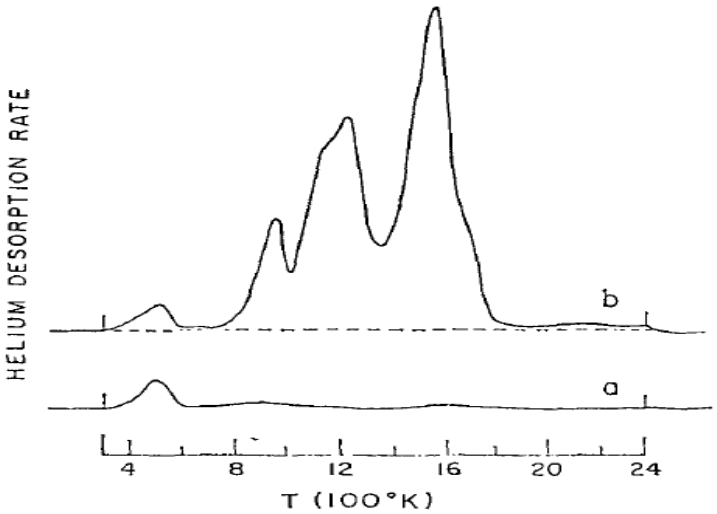

FIG. 2. The general effect of heavy-ion bombardment on the entrapment of helium. In both cases the injected He^+ dose was 2.4×10^{13} ions/cm² at 250 eV: (a) no prior bombardment; (b) prior damaging bombardment: 2.4×10^{11}/cm² 5 keV Kr^+.

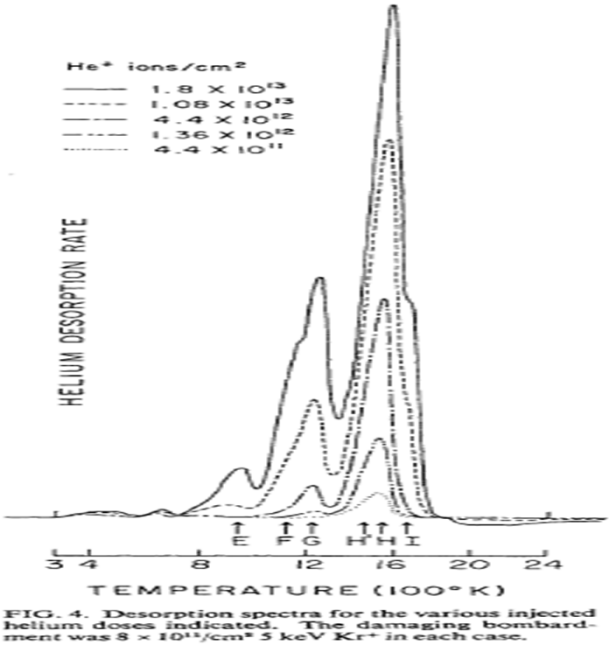

FIG. 4. Desorption spectra for the various injected helium doses indicated. The damaging bombardment was 8×10^{11}/cm² 5 keV Kr^+ in each case.

- He injected into W as 250 eV ions does not itself produce any observable damage
- But He is trapped in that created the prior heavy ion bombardment (Kr, for example)
- TDS shows that He is bound with several discrete energies
- Correlation of binding states with temperature, He doses and the mass of damaging ions

Noble-gas vacancy binding energy trend: Systematic study of electronic structure effects

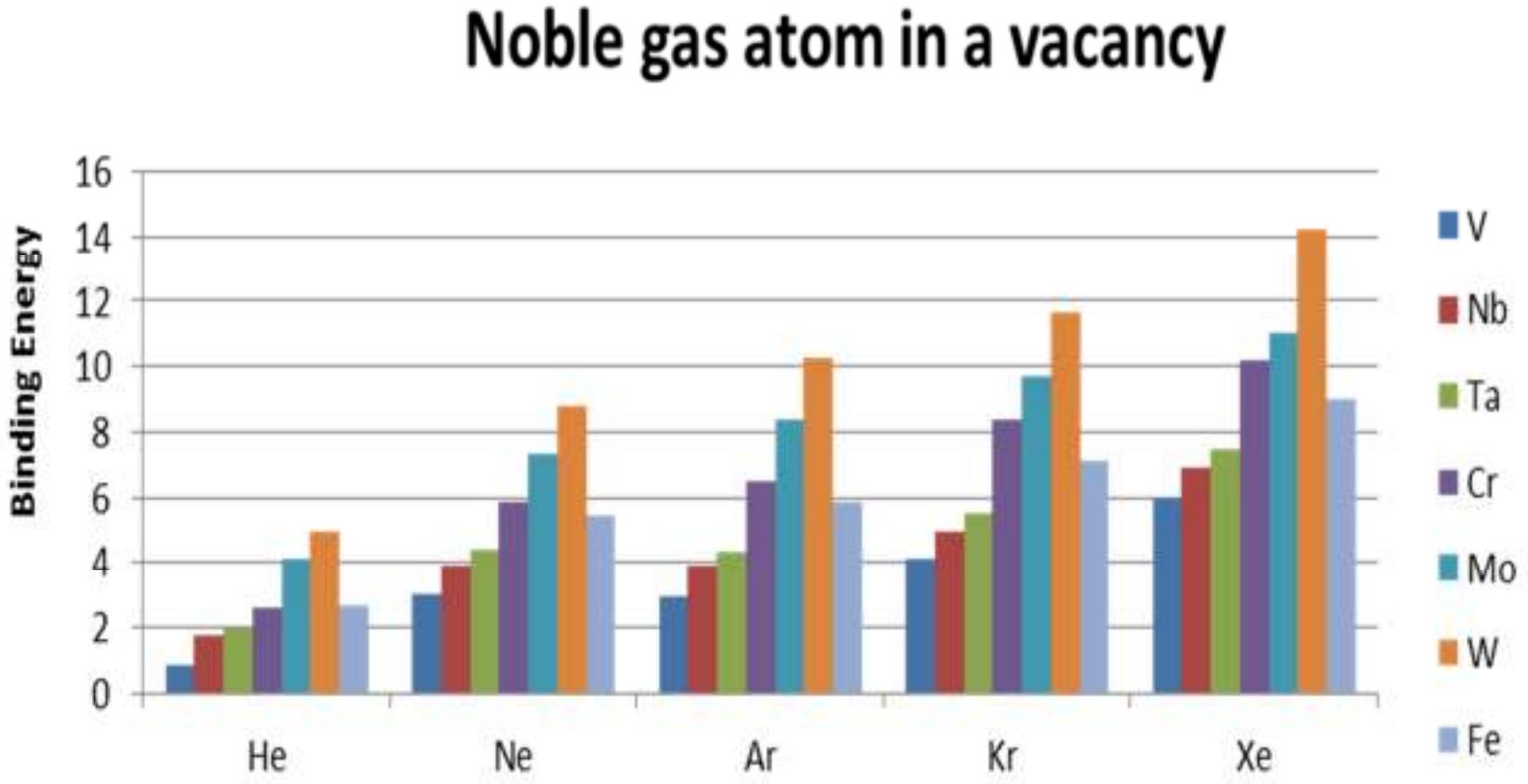

For noble-gas elements in bcc-W: DNM, S.L. Dudarev, NIMB, 352 (2015) 86-91

EUROfusion

WPMAT

Partial DOS for inert-gas (IG) impurities in W: role of p-electrons in IG-v binding energies

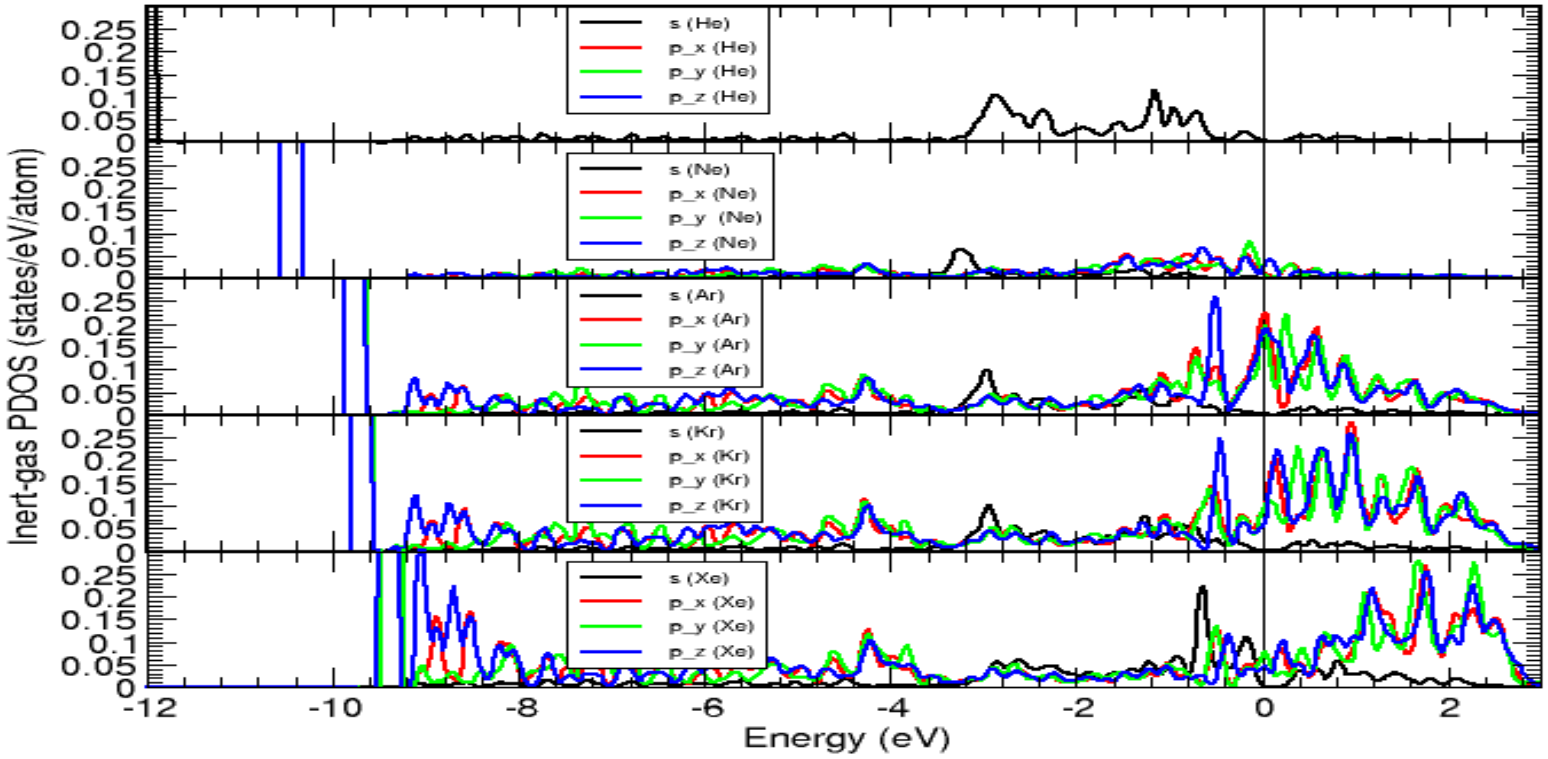

CCFE
CULHAM CENTRE FOR FUSION ENERGY

Trapping of a Helium atom by inert-gas defects: Difference between DFT and Experimental data is small

DFT	EXP
4.63	4.6
3.11	3.1
2.47	2.3
1.93	1.9
1.66	1.5
1.24	1.2

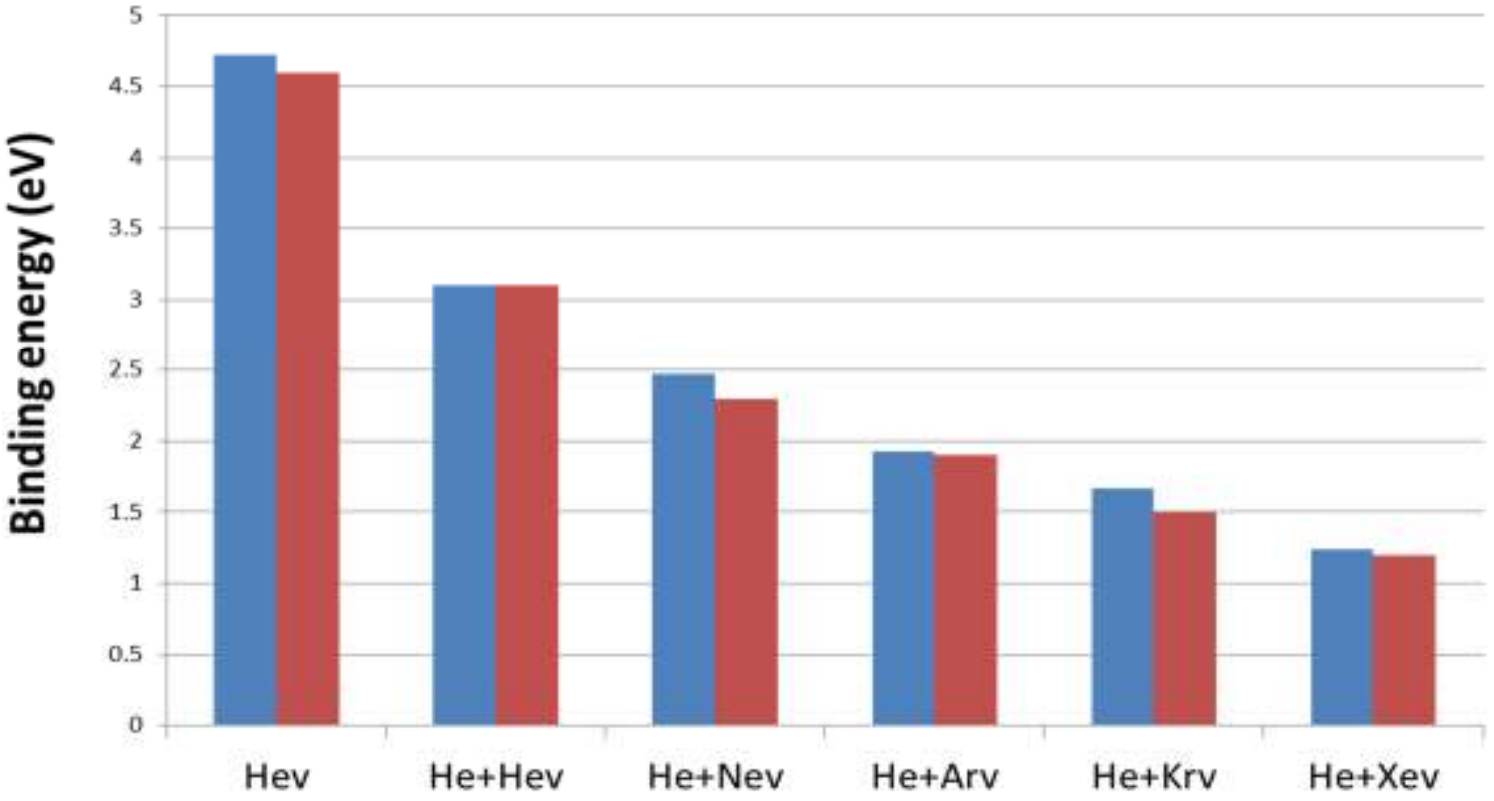

DNM, S.L. Dudarev, NIMB 352 (2015) 86

Experimental data are taken from LANDOLT-BORNSTEIN, vol. 25 (1991)

Experimental validation: Thermal desorption spectrometry

WPMAT

Attachment of He atom to 5 impurity traps: HeV, Ne, Ar, Kr, Xe in bcc-W

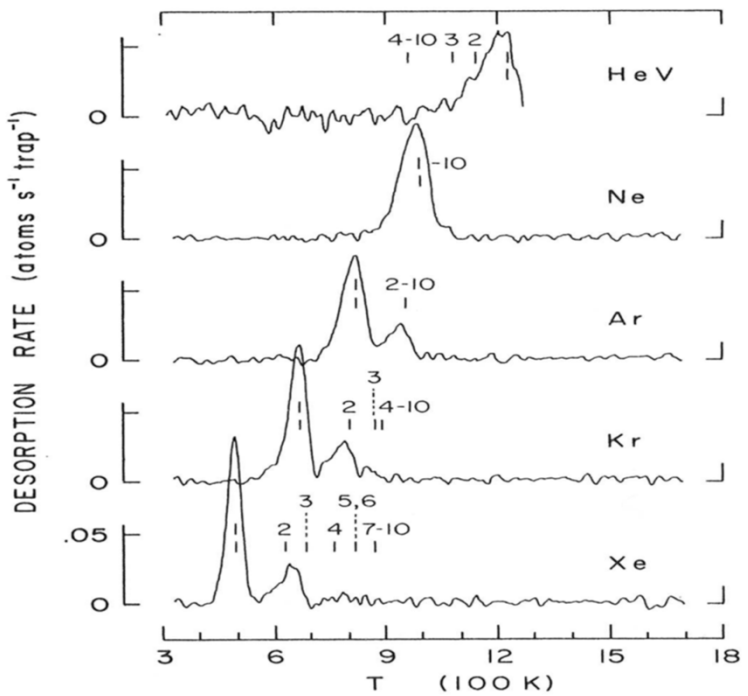

Fig. 1. Desorption spectra from five different trap nuclei. The incident He dose $n^+ = 1 \times 10^{12}/cm^2$, and the average number of trapped He atoms per trap ($\bar{i}$) was about 0.17. The vertical marks on the individual spectra indicate the peak temperatures and the deduced values of the multiplicity i.

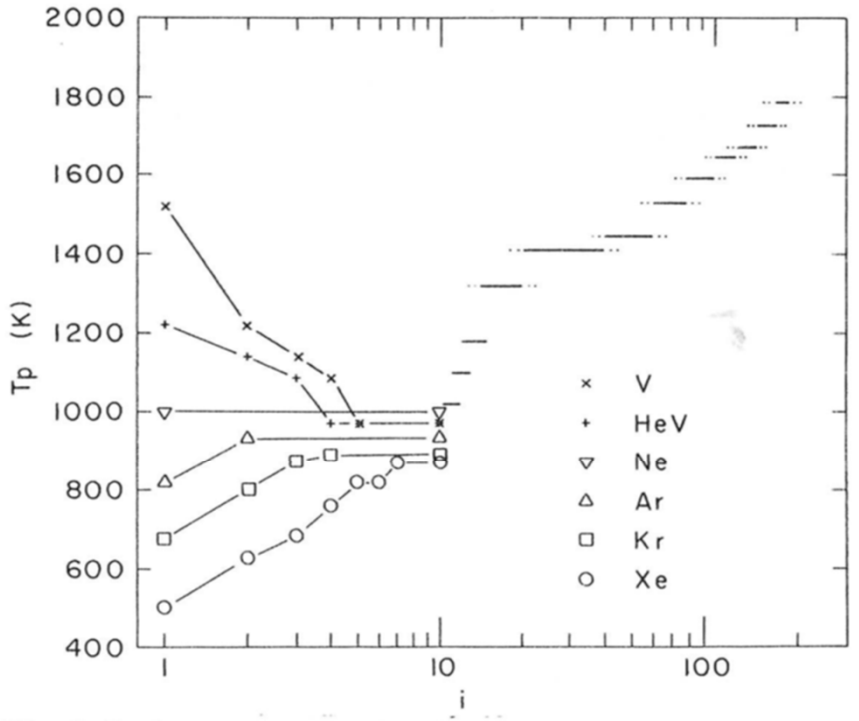

Fig. 7. Peak temperatures for the six trap nuclei as a function of the number i of helium atoms they contain. Above $i = 10$, the bars indicate approximate ranges of the multiplicity i involved in peaks at the indicated temperatures which are the same for all the nuclei.

E.V. Kornelsen and A.A. Van Gorkum, JNM, 92 (1980) 79

EUROfusion

WPMAT

Dissociation energy of a He trapped by (n-1)He-IG-v clusters in bcc-W

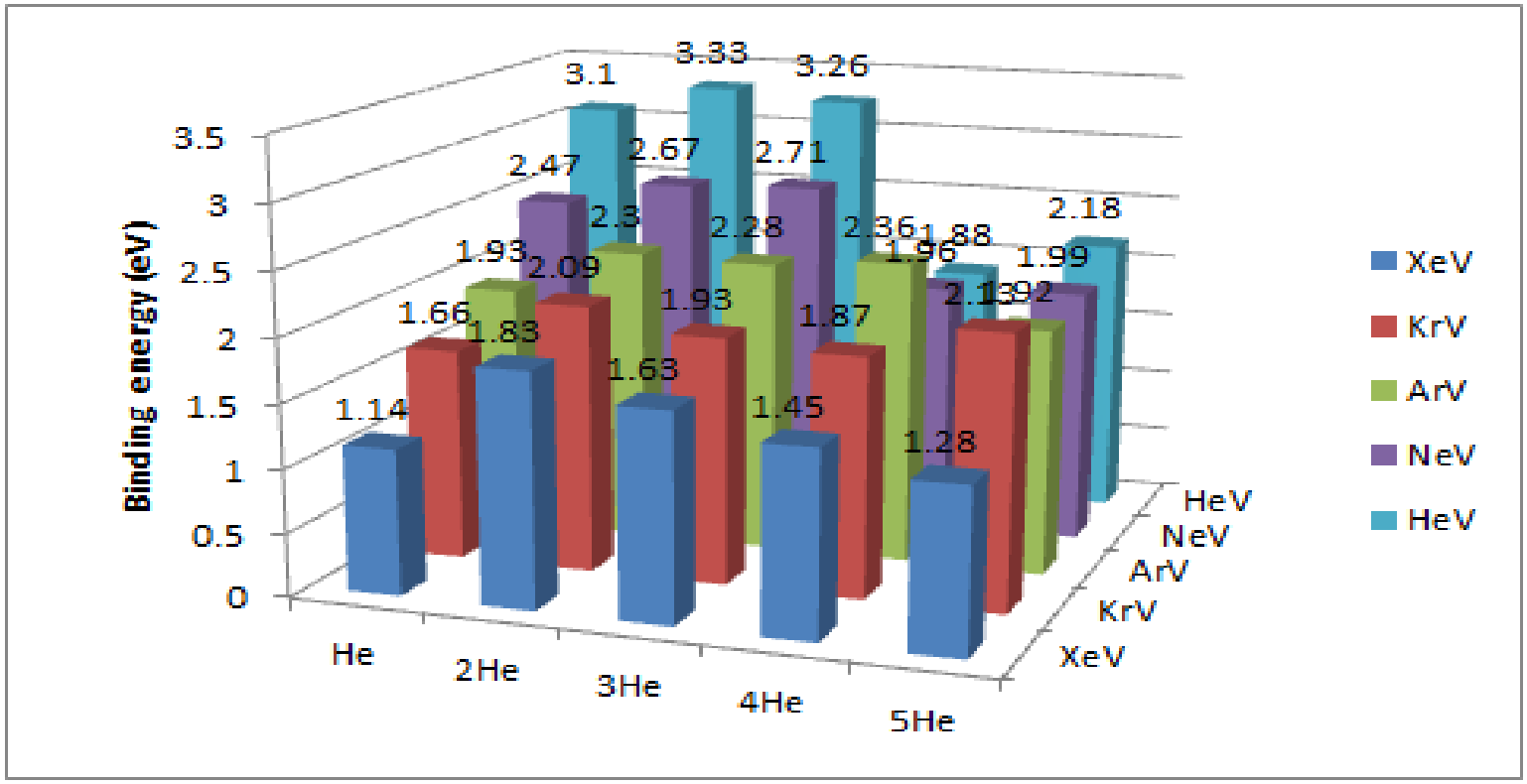

DNM, S.L. Dudarev, Nuc. Ins. Meth. B 352 (2015) 86

CCFE CULHAM CENTRE FOR FUSION ENERGY

EUROfusion

WPMAT

Experimental measurement of lattice swelling and modulus change under irradiation vs. MM validation

ELSEVIER

CrossMark

Available online at www.sciencedirect.com

ScienceDirect

Acta Materialia 89 (2015) 352–363

Acta MATERIALIA

www.elsevier.com/locate/actamat

Lattice swelling and modulus change in a helium-implanted tungsten alloy: X-ray micro-diffraction, surface acoustic wave measurements, and multiscale modelling

F. Hofmann,[a,*] D. Nguyen-Manh,[b,c] M.R. Gilbert,[b,c] C.E. Beck,[c] J.K. Eliason,[d] A.A. Maznev,[d] W. Liu,[e] D.E.J. Armstrong,[c] K.A. Nelson[d] and S.L. Dudarev[b,c]

[a]*Department of Engineering Science, University of Oxford, Parks Road, Oxford OX1 3PJ, UK*
[b]*CCFE, Culham Science Centre, Abingdon OX14 3DB, UK*
[c]*Department of Materials, University of Oxford, Parks Road, Oxford OX1 3PH, UK*
[d]*Department of Chemistry, Massachusetts Institute of Technology, 77 Massachusetts Avenue, Cambridge, MA 02139, USA*
[e]*Advanced Photon Source, Argonne National Lab, 9700 South Cass Avenue, Argonne, IL 60439, USA*

EUROfusion

WPMAT

Measurements of elastic properties and lattice swelling

Surface Acoustic Wave Measurements:

Measuring elastic properties of the He-implanted layer:

- Transient grating (TG), λ = 2.75 µm, made by overlapping two pump beams: 515 nm, 60 ps, 1.75 µJ /pulse, spot: 500 µm [9].
- TG generates two counter-propagating surface acoustic waves (SAWs). Probe SAWs by scattering of a quasi CW probe beam: 532 nm, 10 mW, spot: 300 µm.
- SAW velocity: unimplanted material: 2679 ± 2 ms^{-1}
  He-implanted material: 2621 ± 7 ms^{-1} (-2.2 %)

$$c_r = f\lambda \approx \left(0.874 + 0.196\nu - 0.043\nu^2 - 0.055\nu^3\right)\sqrt{\frac{E}{2(1+\nu)\rho}}$$

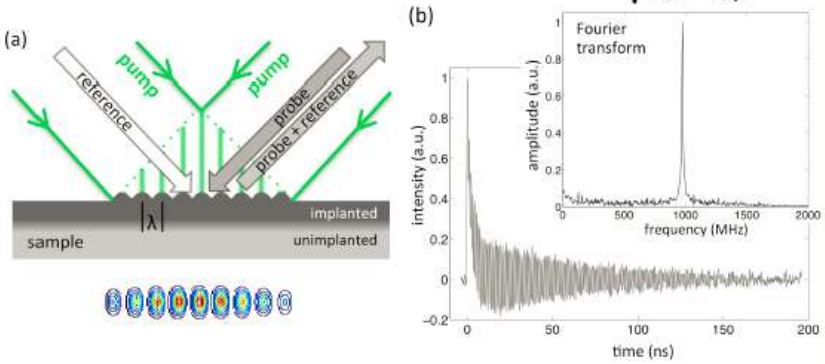

Synchrotron X-ray Micro Diffraction:

Measuring lattice swelling of the He-implanted layer:

34-ID-E @ APS

- Polychromatic (7-30 keV) and Monochromatic (ΔE/E ~ 10^{-4}) DAXM
  => depth-resolved full strain tensor [10].
- Beam size: 0.6 (h) x 0.4 (v) µm².
- Depth resolution: ≈ 0.5 µm.
- In-plane strains ≈ 0
  => no bubbles.
- Swelling of He-implanted surface layer:

$$\varepsilon_{zz} = \frac{\varepsilon_v}{3} + 2\frac{\nu}{(1-\nu)}\frac{\varepsilon_v}{3}$$

$$\varepsilon_{zz} = (1550 \pm 120) \times 10^{-6}$$

$$\varepsilon_v = (2620 \pm 200) \times 10^{-6}$$

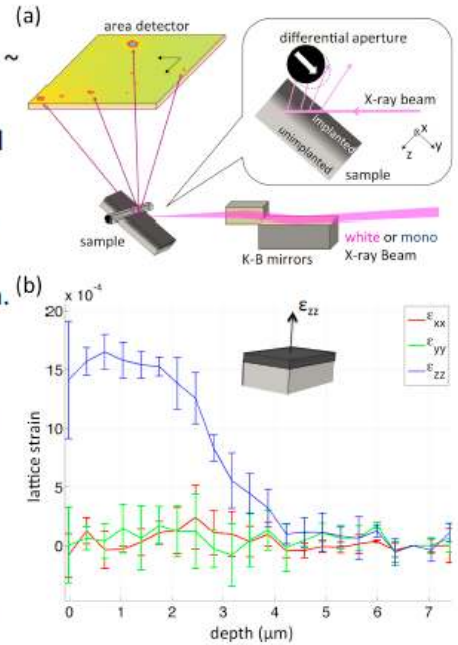

3100 apmm He implanted

From continuum elasticity to atomic-level stresses

A defect in an isotropic elastic medium (tungsten is elastically isotropic) generates a field of atomic displacements of the form [54],

$$u_i^{(\alpha)} = -P_{ks}^{(\alpha)} \frac{\partial}{\partial x_s} G_{ik}(\mathbf{r} - \mathbf{R}_\alpha), \tag{A1}$$

where $\mathbf{R}_\alpha$ is the position vector of a defect and $P_{ks}^{(\alpha)}$ is the defect's dipole tensor, corresponding to the density of forces of the form $f_k(\mathbf{r}) = -P_{ks}^{(\alpha)} \frac{\partial}{\partial x_s}\delta(\mathbf{r})$. For an ensemble of defects the density of forces is given by the sum over all the defects in the material

$$F_k(\mathbf{r}) = -\sum_\alpha P_{ks}^{(\alpha)} \frac{\partial}{\partial x_s}\delta(\mathbf{r} - \mathbf{R}_\alpha). \tag{A2}$$

The elastic stress tensor satisfies the equilibrium condition [76]:

$$\frac{\partial}{\partial x_j}\sigma_{ij} + F_i(\mathbf{r}) = 0, \tag{A3}$$

and is related to the elastic strain tensor ε_{ij} through the equation [76]:

$$\sigma_{ij} = \frac{E}{1+v}\left(\varepsilon_{ij} + \frac{v}{1-2v}\varepsilon_{ll}\delta_{ij}\right). \tag{A4}$$

The accumulation of anisotropic defects in the implanted layer could give rise to non-vanishing x,y components of force in the plane of the surface. In the absence of direct experimental evidence for such forces, we only consider the z-component of the density of forces:

$$F_z(\mathbf{r}) = F_z(z) = -\sum_A n^{(A)} P_{zz}^{(A)}(\delta(z) - \delta(z-L))$$

$$= -\frac{1}{3}\sum_A n^{(A)}\mathrm{Tr}(P_{ij}^{(A)})(\delta(z) - \delta(z-L)). \tag{A8}$$

The use of trace of defect dipole tensor stems from the fact that defects adopt random orientations in the implanted layer. The formula can be simplified if we note [56] that $\mathrm{Tr}(P_{ij}^{(A)}) = \frac{E}{1-2v}\Omega_r^{(A)}$, where $\Omega_r^{(A)}$ is the relaxation volume of a defect of type A.

The elastic equilibrium conditions have the form [76]:

$$\frac{\partial}{\partial z}\sigma_{zz} + F_z(z) = 0; \quad \frac{\partial}{\partial z}\sigma_{xz} = \frac{\partial}{\partial z}\sigma_{yz} = 0. \tag{A9}$$

At the free surface $z = 0$ we supplement them with the traction-free boundary conditions $\sigma_{xz}(z=0) = \sigma_{yz}(z=0) = \sigma_{zz}(z=0) = 0$ and find,

$$\frac{\partial}{\partial z}\sigma_{zz} = \frac{1}{3}\sum_A n^{(A)}\mathrm{Tr}(P_{ij}^{(A)})(\delta(z) - \delta(z-L)), \tag{A10}$$

$$\sigma_{zz} = \frac{1}{3}\sum_A n^{(A)}\mathrm{Tr}(P_{ij}^{(A)})(\Theta(z) - \Theta(z-L)). \tag{A11}$$

UQ: From DFT to Experimental Data

Density Functional Theory Modelling:

- Central defect in 4 x 4 x 4 tungsten BCC supercell => 128 atoms.
- Periodic boundaries, free to expand.

Lattice swelling - Relaxation volume calculations:

- Estimate relaxation volume: $\Omega_r(\text{defect}) = \Omega(\text{defect}) - \Omega(\text{perfect})$
- Estimate lattice swelling: $\varepsilon_v = \sum_A n_A \Omega_r^{(A)}$ and $\varepsilon_{zz} = \frac{1}{3}\frac{(1+\nu)}{(1-\nu)}\sum_A n_A \Omega_r^{(A)}$
- If we assume 1 He per V: predict ε_{zz} (HeV) = 2654 x 10^{-6} => ~ twice experimental ε_{zz}.
- Consider clustering [11]: 1555 appm He_2V complexes & 1555 appm SIAs: predict ε_{zz} (He_2V) = 1493 x 10^{-6} => **very good agreement with experimental ε_{zz} strain.**

Relaxation volumes for vacancies and self-interstitial

V	V_2 (1NN)	V_2 (2NN)	V_2(3NN)	V_3(1NN(2) +2NN)	<111> SIA	Frenkel
-0.37 -0.34 [a] -0.38 [b]	-0.72 -0.65 [a]	-0.79 -0.74 [a]	-0.76 -0.69 [a]	-1.08	1.68	1.31

Relaxation volumes for interstitial helium clusters

He (tetra)	He (octa)	He_2 (tetra)	He_3 (tetra)	He_4 (tetra)	He_5 (tetra)
0.36 0.33 [c]	0.37 0.34 [c]	0.80	1.16	1.65	2.03

Relaxation volumes for helium - vacancy clusters

HeV (tetra)	HeV (octa)	He_2V (tetra)	He_3V (tetra)	He_4V (tetra)	He_5V (tetra)	He_6V (tetra)
-0.24	-0.23	-0.06	0.14	0.38	0.71	1.09

[a] Kato D, Iwakiri H, Morishita K. Journal of Nuclear Materials 2011;417:1115.
[b] Heinola K, Ahlgren T, Nordlund K, Keinonen J. Physical Review B 2010;82:094102.
[c] Zhou HB, Jin S, Shu XL, Zhang Y, Lu GH, Liu F. EPL (Europhysics Letters) 2011;96:66001.

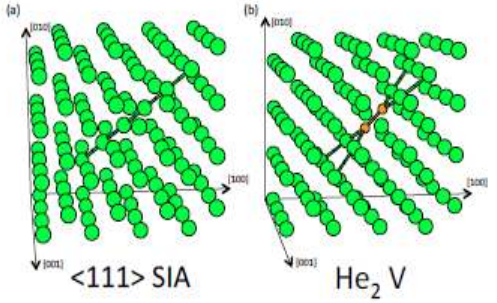

Calculation details:
Perdew-Burke-Ernzerhof electron exchange-correlation functional within generalized gradient approximation. Projector augmented wave (PAW) pseudopotentials implemented in the Vienna Ab-initio Simulation Package (VASP). 400 eV plane wave cutoff energy and 4 x 4 x 4 k-point mesh with 0.15 Å^{-1} spacing. Periodic boundary conditions with expansion in all directions allowed.

Modulus change calculations:

- Calculate elastic constants for different defects.
- Estimate SAW velocity change due to He-implantation: predicted (-1.8%) experimental (-2.2%)

=> excellent agreement; no free parameters.

		C_{11} (GPa)	C_{12} (GPa)	C_{44} (GPa)	A
Pure W experimental at 298 K [12-14]		522.8	203.5	160.7	1.01
Pure W	from DFT	537.4	188.2	153.7	0.88
	rescaled	522.8	203.5	160.7	1.01
W + SIA	from DFT	512.5	212.5	141.4	0.94
	rescaled	498.6	229.8	147.8	1.10
W + He_2V	from DFT	518.9	188.1	141.2	0.85
	rescaled	504.8	203.4	147.6	0.98

$$C_{ij}^{implanted} = (1 - 128(n_{SIA} + n_{He_2V}))C_{ij}^{W} + 128 n_{SIA} C_{ij}^{SIA} + 128 n_{He_2V} C_{ij}^{He_2V}$$

	A	K (GPa)	G (GPa)	E (GPa)	nu
Pure W	1.01	309.9	160.3	410.1	0.279
W + 1555 appm He_2V + 1555 appm SIAs	1.02	310.6	154.5	397.5	0.287

Predicted SAW velocities

in m/s	rescaled		direct from DFT		experiments
	Voigt	Reuss	Voigt	Reuss	
Perfect W	2667	2667	2680	2675	2679
W + He_2V + SIAs	2622	2618	2636	2628	2621
Change	-1.7%	-1.9%	-1.7%	-1.8%	-2.2%

EUROfusion

WPMAT

Micro-structural evolution in W&W alloys under irradiation

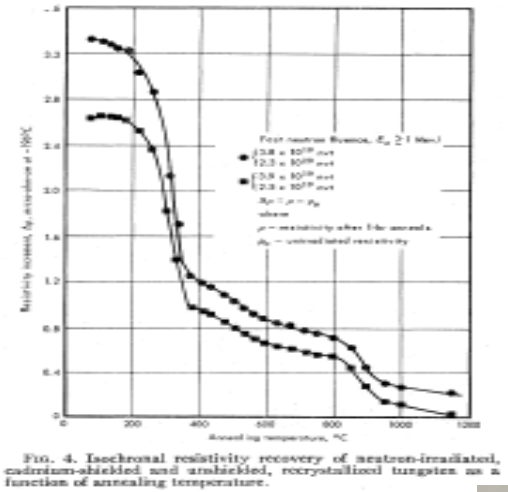

FIG. 4. Isochronal resistivity recovery of neutron-irradiated, cadmium-shielded and unshielded, recrystallized tungsten as a function of annealing temperature.

High-temperature recovery in W after neutron irradiation (Stage IV and V ???) L.K. Keys et al. Phys. Rev. 176 (1968) 851

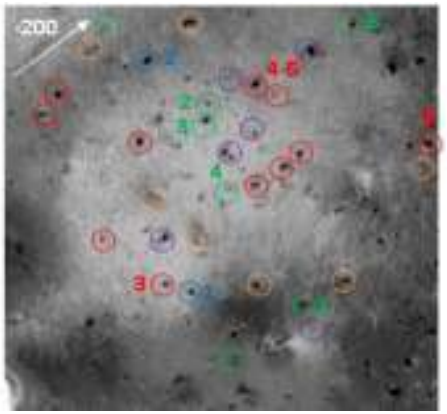

Evidence of vacancy loops in irradiated tungsten (2 MeV W^+, T = 300° C, 10^{14} W^+/cm^2) Xiaoou Yi (2004)

Vacancy clusters & He-vac interaction and W, Fe & Fe alloys (PAS, NRA, TEM)

M-F Barthe et al. , May 26th 2015

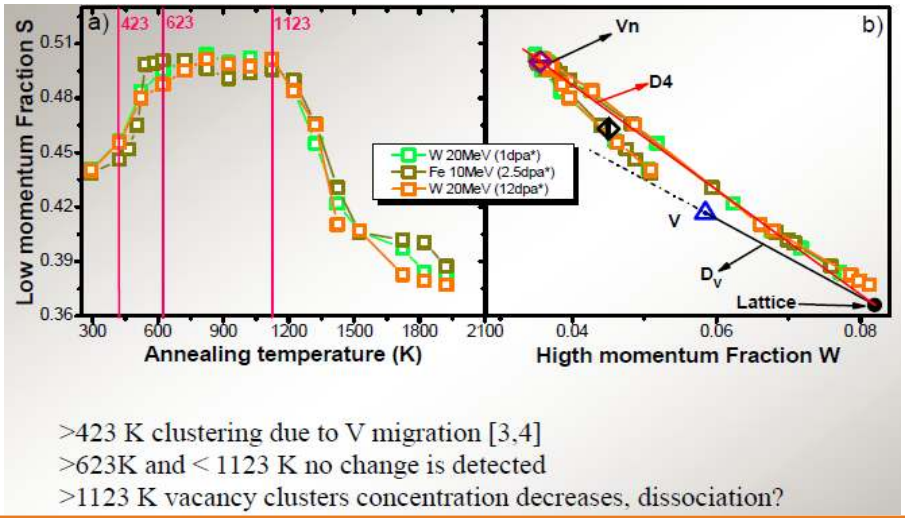

➢ ***Micro-structural evolution associate with Formation of vacancy cluster, stable configurations, binding energies, activation energies of transition, migration process at high temperature***

EUROfusion

WPMAT

Neutron irradiation in Tungsten

Irradiated in JOYO

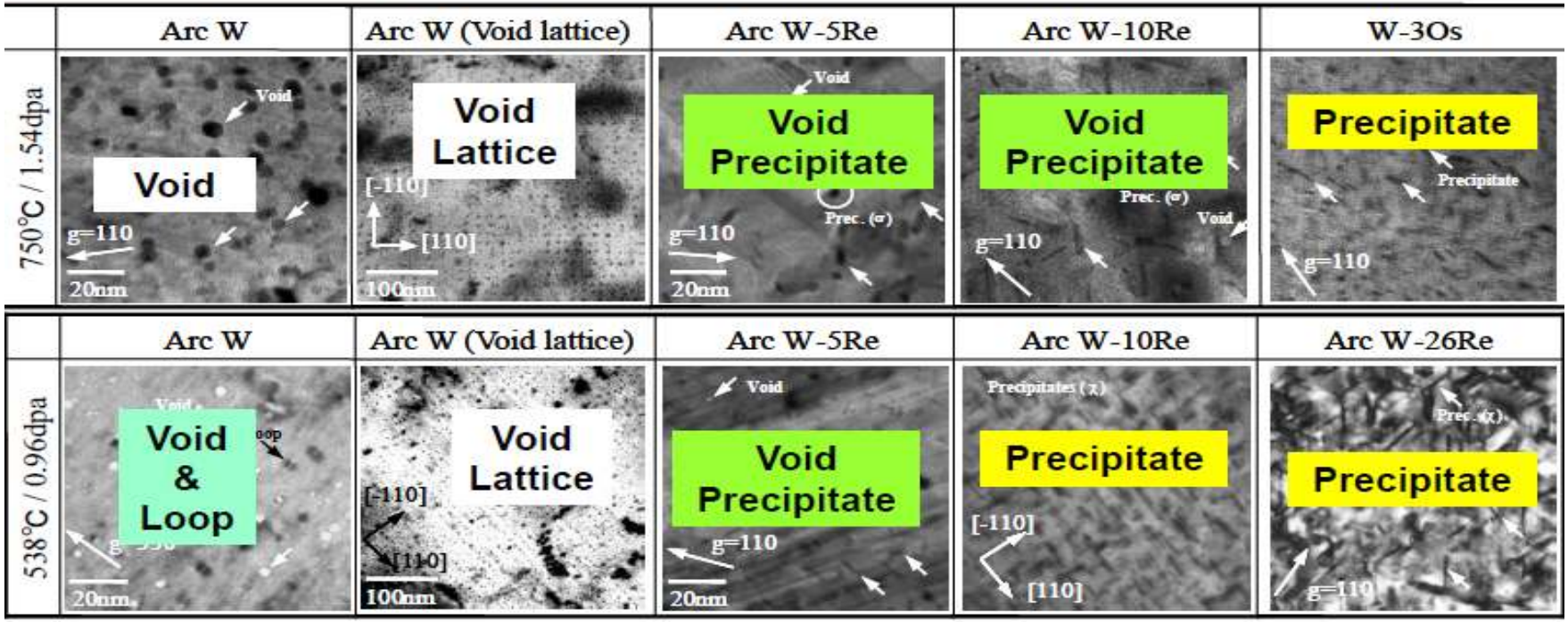

Void lattice were observed in pure W. (pure W → W-1.5Re-0.05Os after 1.5dpa)

Void formation was drastically suppressed in W-Re and acicular precipitates were observed above 5%Re.

T. Tanno, A. Hasegawa

SIA loops loss and void formation at high temperature

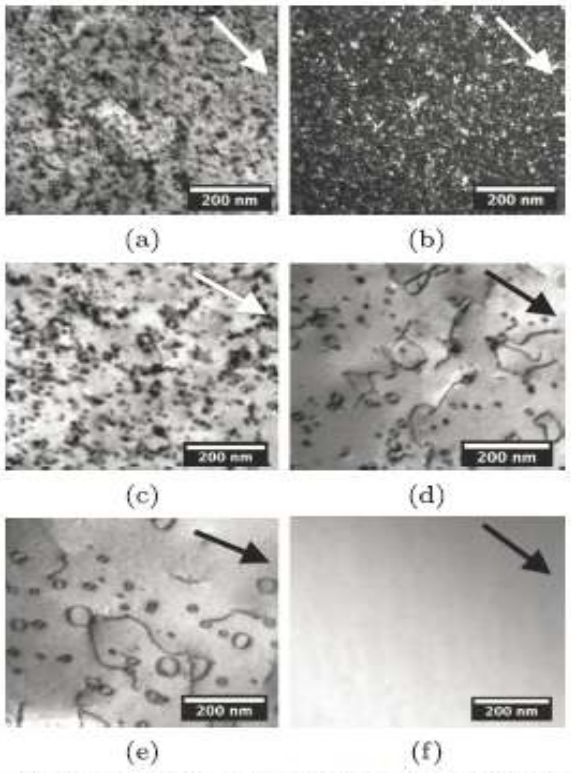

Fig. 1. Damage microstructure in (a and b) as-irradiated tungsten (1.5 dpa, 2 MeV W+, 500 °C) and post-irradiation annealed tungsten subject to conditions of (c) 800 °C for 1 h, (d) 950 °C for 1 h, (e) 1100 °C for 1 h, (f) 1400 °C for 1 h. All micrographs shown were imaged close to [001], with $g = (200)$ excited. The arrow in each micrograph shows the direction of the g-vector. (b) is weak-beam dark-field (g, 3–4g), to pick-up the diffraction contrast of very small loops, 1–2 nm. (a) and (c–e) are two-beam kinematical bright-field images.

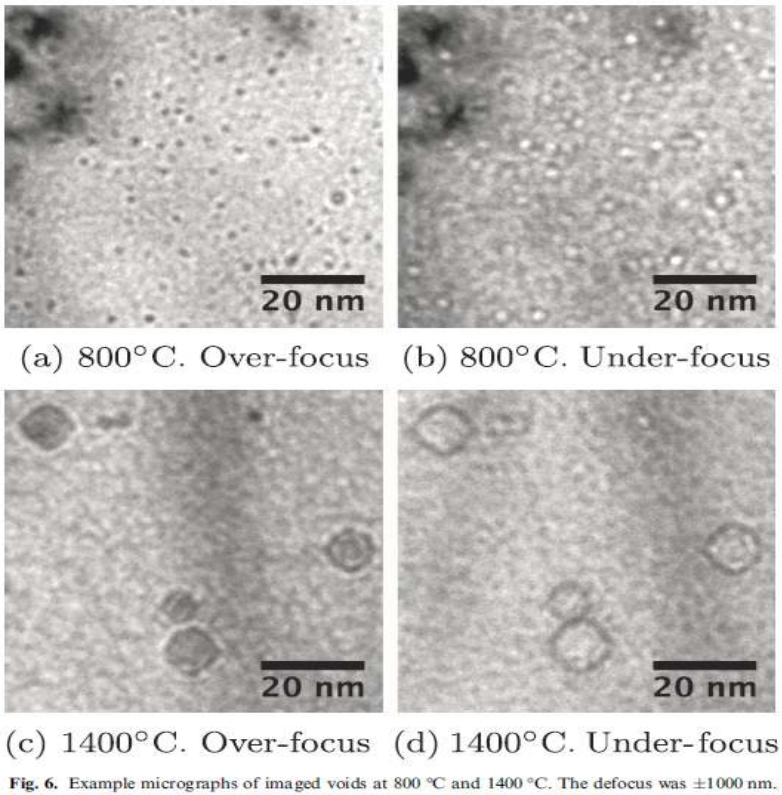

Fig. 6. Example micrographs of imaged voids at 800 °C and 1400 °C. The defocus was ±1000 nm.

F. Ferroni, Acta Mat. 90 (2015) 380; Isothermal and isochronal annealing of 2MeV irradiated W, 500C-1200C, 10^14 W+/cm2

EUROfusion

WPMAT

Surface effects for exchange & correlation (XC) energies in first-principles modelling

- An apparent inability of DFT within LDA and GGA to describe vacancy formation energy accurately not only in bcc metals (recent DFT data 3.0-3.3 eV w.r.t cell sizes, k-points …whereas experimental values are 3.5-4.0 eV in bcc-W) but also in fcc metals such as Al…
- Theoretical treatment of electronic surfaces – i.e., strongly inhomogeneous electron density is the weakness of popular functionals.

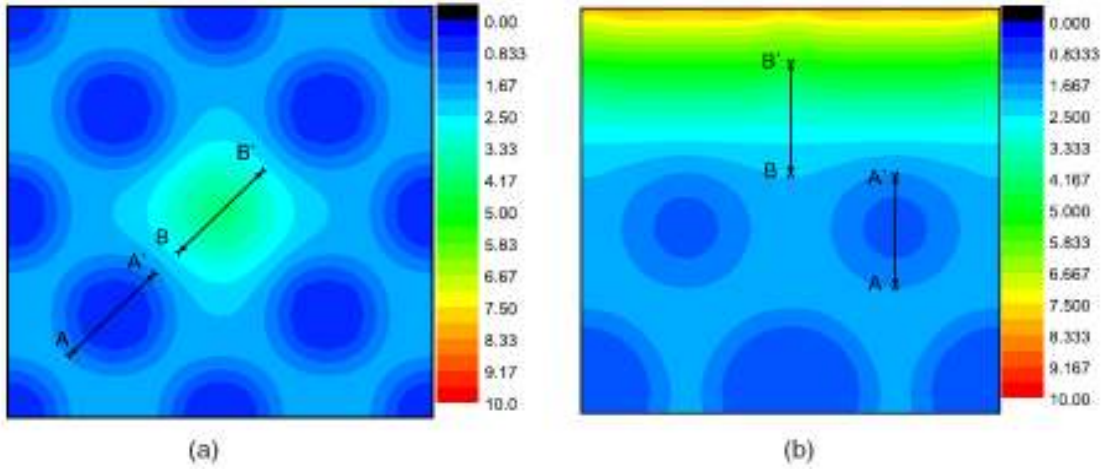

L. Vitos et al., PRB 62 (2000) 10046; R. Armiento, A.E. Mattsson, PRB, 72 (2005) 065108 (**AM05**): treatment of electron gas at surface and interior Region. Could AM05 be better than LDA and PBE for solids (J. Chem. Phys. 128 (2008) 084714?

Density parameter: electron radius r_s

EUROfusion

WPMAT

AM05 calculations for vacancy clusters

- M. Muzyk, DNM, K.J. Kurzydlowski, N.L. Baluc, S.L. Dudarev, PRB, 84, 104115 (2011)
- Cross checking empirical potentials calculations (Ref. 71) T. Ahlgren et al. JAP 107(2010) 033516
- DFT predicted a lower energy 5-vacancy cluster configuration

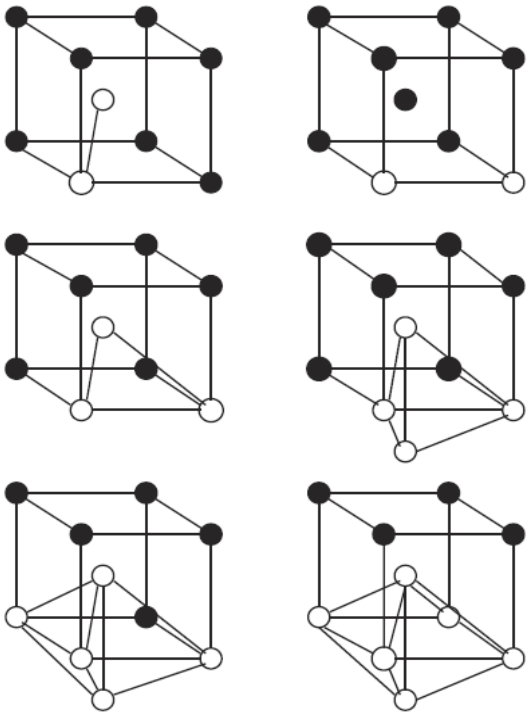

FIG. 12. Tungsten vacancy cluster configurations ($N_v = 2-6$) investigated in the present study.

TABLE III. Formation energies (E_f) and binding energies (E_b), in eV, of vacancy clusters in tungsten. Positive values of the binding energy indicate attraction between the vacancies, leading to clustering of vacancies, whereas negative values indicate repulsion.

Cluster	PBE E_f	PBE-AM05 E_f	PBE E_b	PBE-AM05 E_b
1	3.327	3.568		
2 ((111))	6.624	7.129	0.029	0.007
2 ((100))	6.989	7.325	−0.365	−0.190
3	9.711	10.454	0.269	0.250
4	12.242	13.398	1.065	0.874
5	14.669	16.103	1.965	1.736
5 (Ref. 71)	15.744	17.230	0.890	0.610
6	17.847	19.457	2.113	1.950

- I. Ventelon et al. JNM 425 (2012) 16: SIA and di-vacancy in bcc TMs
- D. Kato et al., Nov. 2014 IAEA-ICTP Conference: Multiple H trapping by vacancies in W

EUROfusion

WPMAT

Surface effects implemented in corrected Ackland-Thetford (AT) potentials for bcc-W

- The potential has been re-fitted to better reproduce known vacancy clusters (1-6) in tungsten. In particular it reproduces surface energies and small vacancy clusters (di-vacancy and tri-vacancy) reasonably well in a comparison with DFT data.
- The AT embedding functional is corrected at the low electron density region
- Electron, phonon entropies and thermal conductivity at finite T are investigated by D. Mason
- Repulsive pair potentials are also modified to avoid discontinuous second derivatives (fitted to higher-order polynomials)

Corrected AT potential prediction for nano-cluster of vacancies

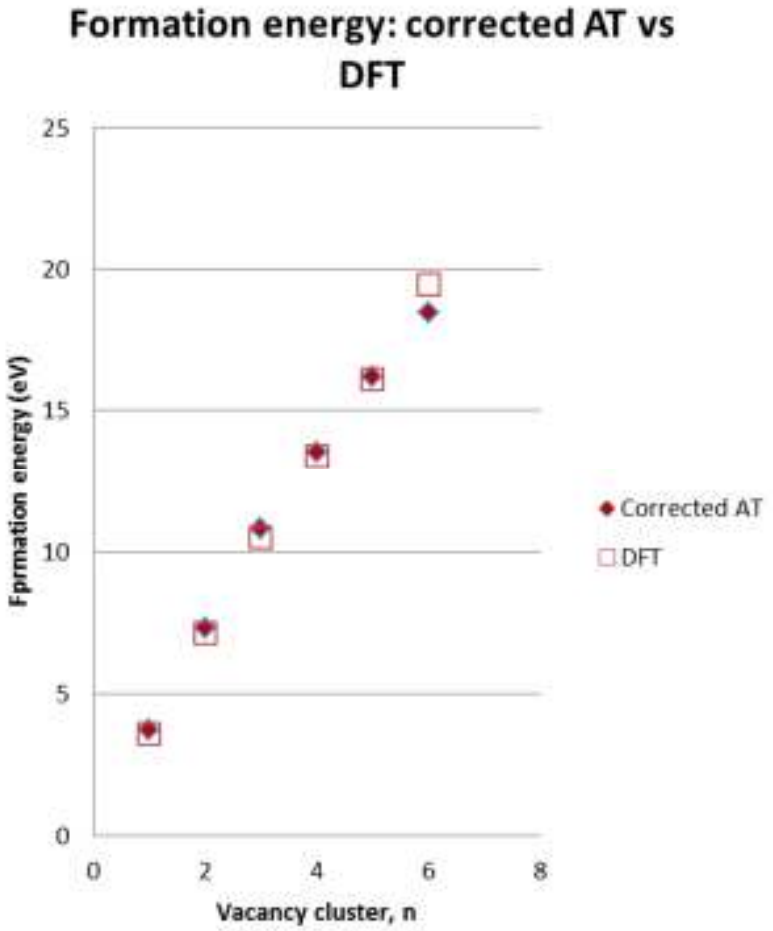

- Number of different possible configuration (M) that number of vacancies (n) can be arranged in N lattice positions increases for large cluster: $M=N*(N-1)*\ldots(N-n+1)/n$
- The procedure to generate vacancy cluster is based on a simulated annealing search
- DFT calculations were performed for vacancy cluster configurations generated by corrected AT potentials

EUROfusion

WPMAT

Formation energies for 1-10 vacancy clusters in bcc-W

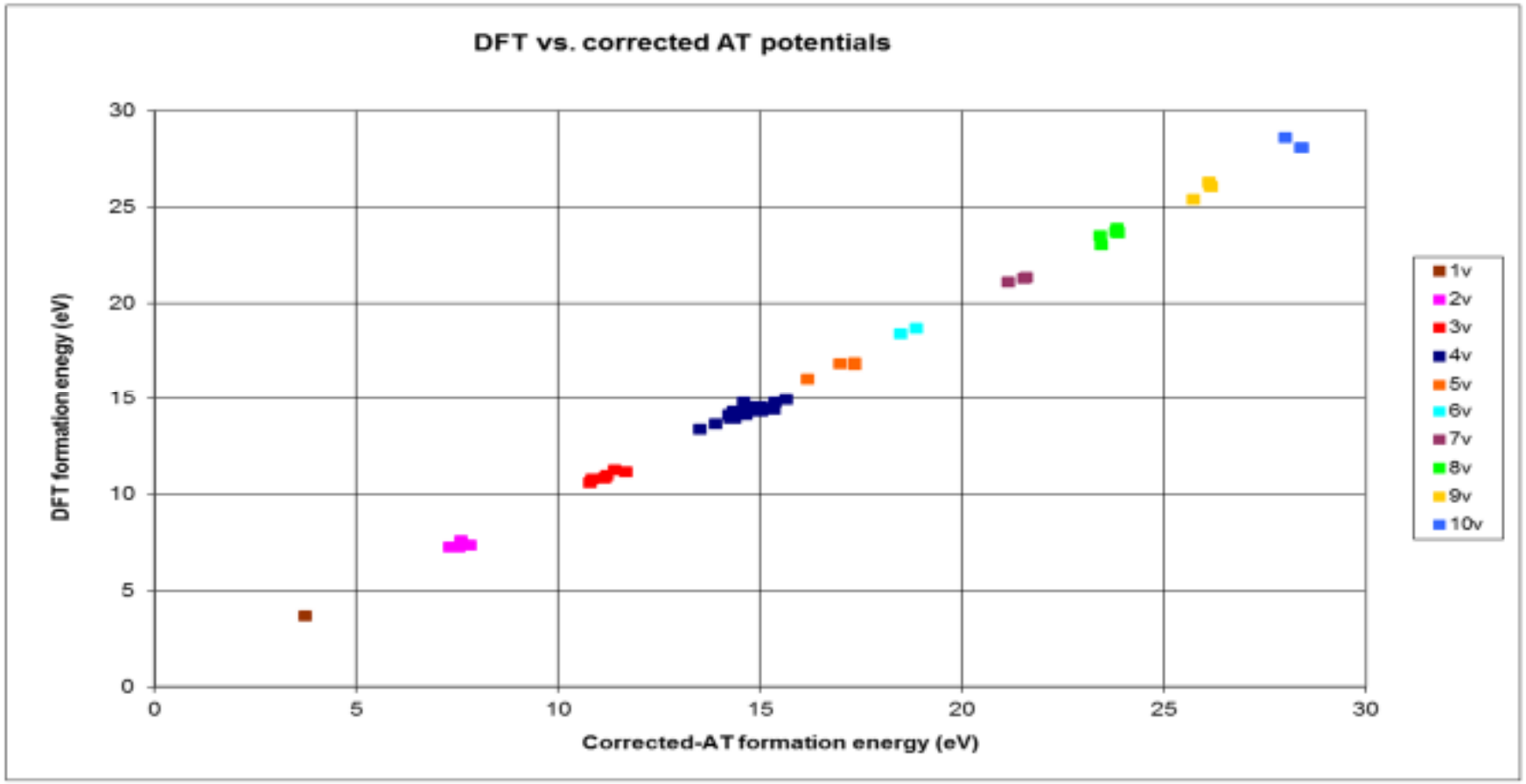

EUROfusion

WPMAT

Low-energy configuration prediction (1-15)

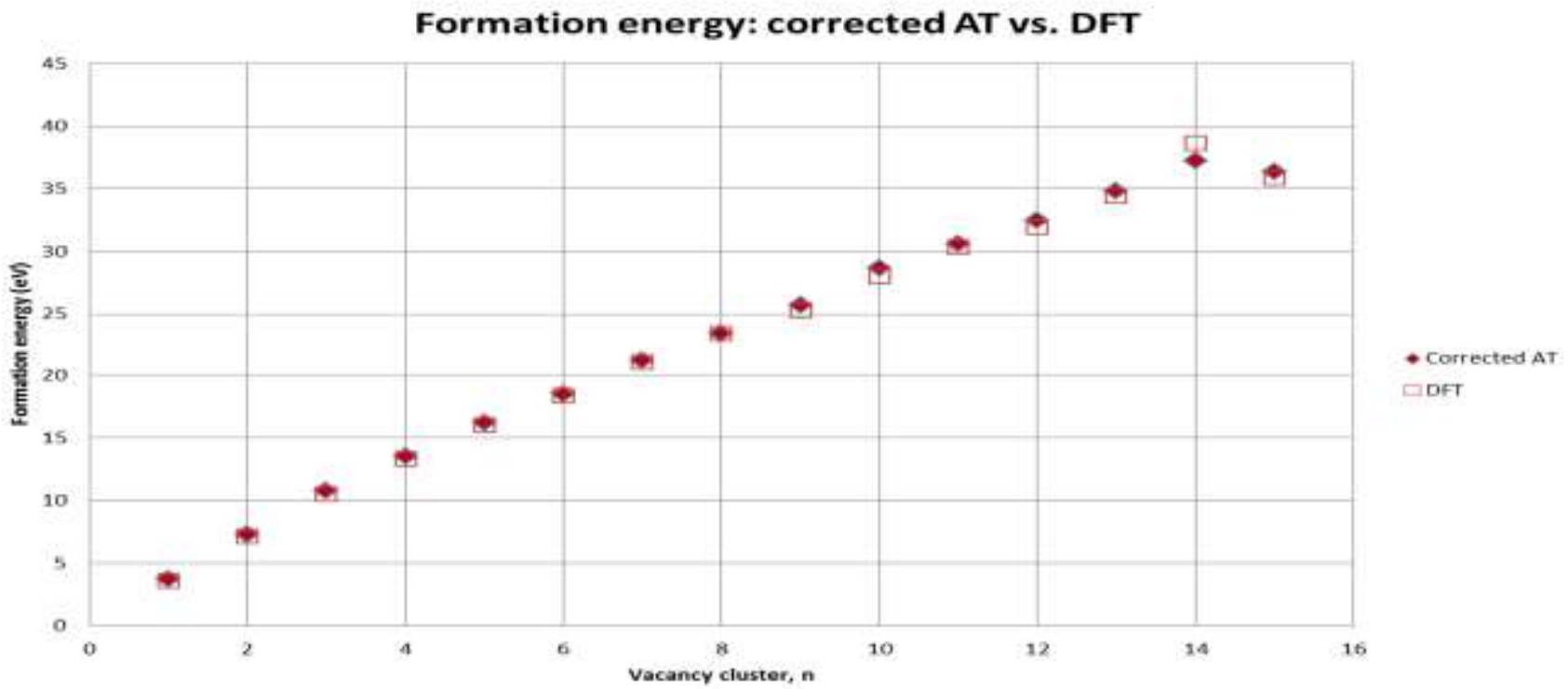

For 15-vacancy cluster, the <110> facetted dodecahedral configuration is the most stable one

EUROfusion

WPMAT

Vacancy nano-clusters stability from electronic structure calculations

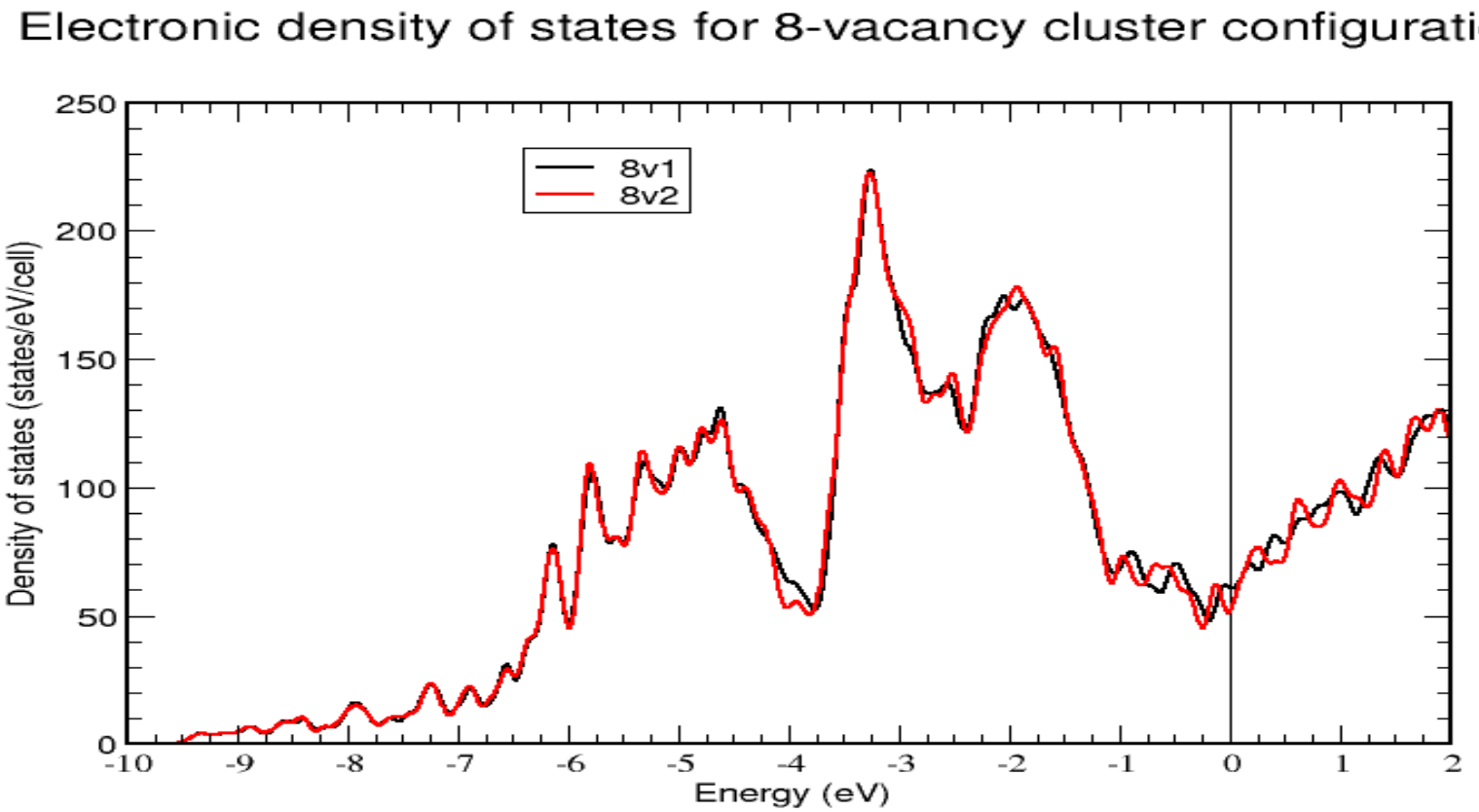

8v1: 23.426 eV (DFT) 23.429 eV (Corr-AT); 8v2: 22.958 eV (DFT) 23.467 eV (Corr-AT)

EUROfusion

WPMAT

Surface effect of formation energies

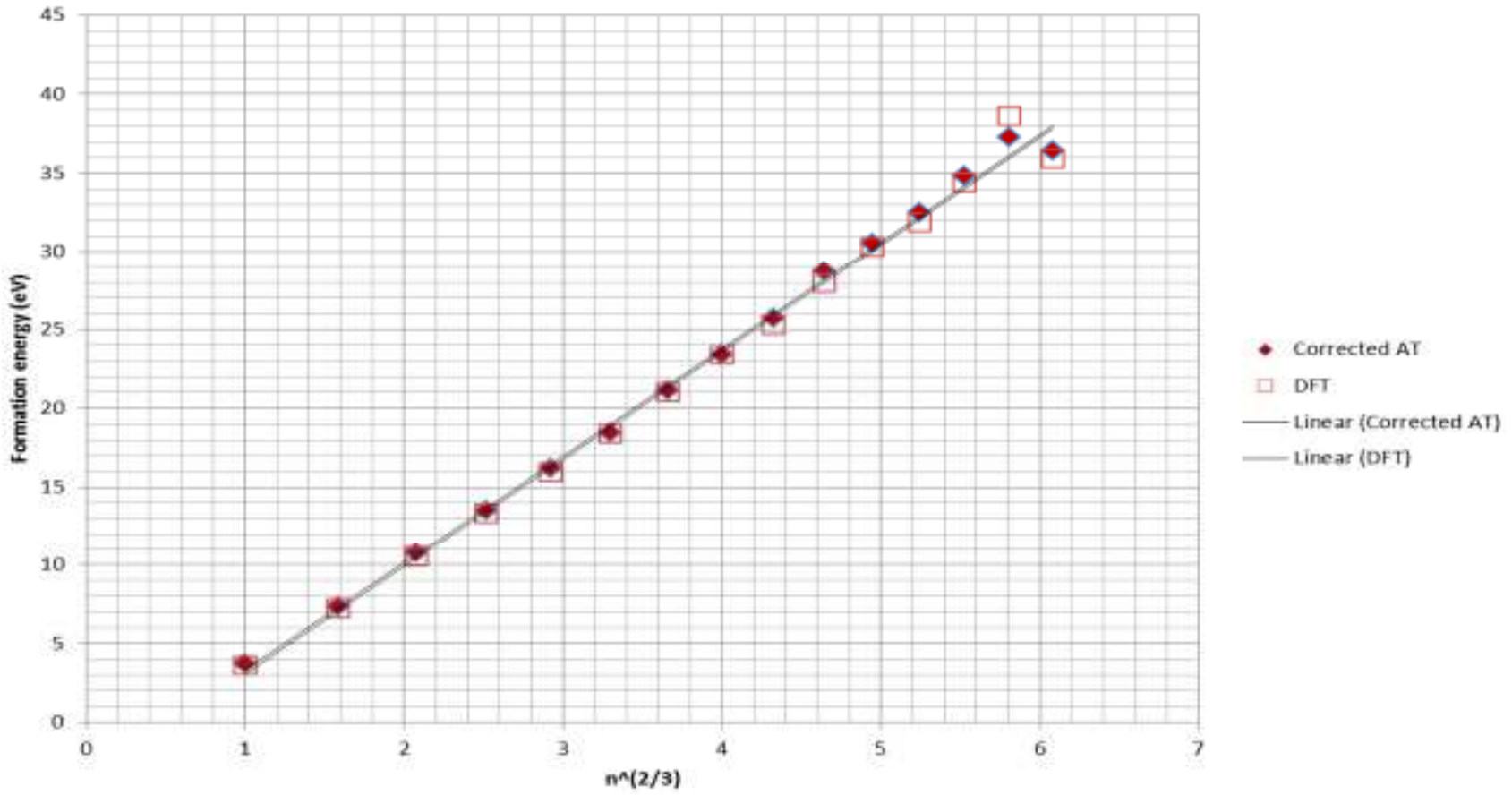

EUROfusion

WPMAT

Volume relaxation of vacancy clusters

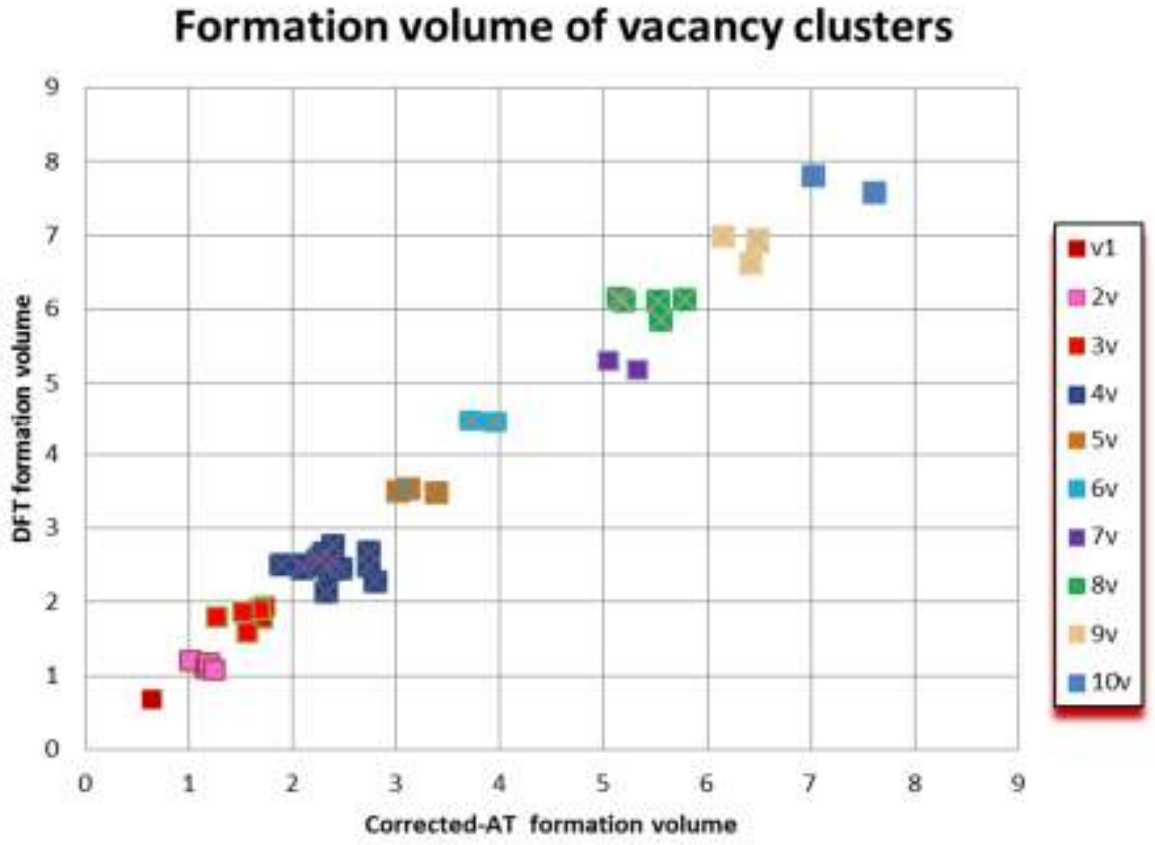

Importance of defect volume relaxation in understanding of swelling effect in He-implanted tungsten from multi-scale modelling

F. Hofmann, DNM, M. Gilbert, C.E Beck, J.K. Eliason, A.A. Maznev, W. Liu, D. Armstrong, K.A. Nelson, S.L. Dudarev
Acta Mat. 89 (2015) 352

EUROfusion

WPMAT

Migration energies: DFT vs. corrected AT

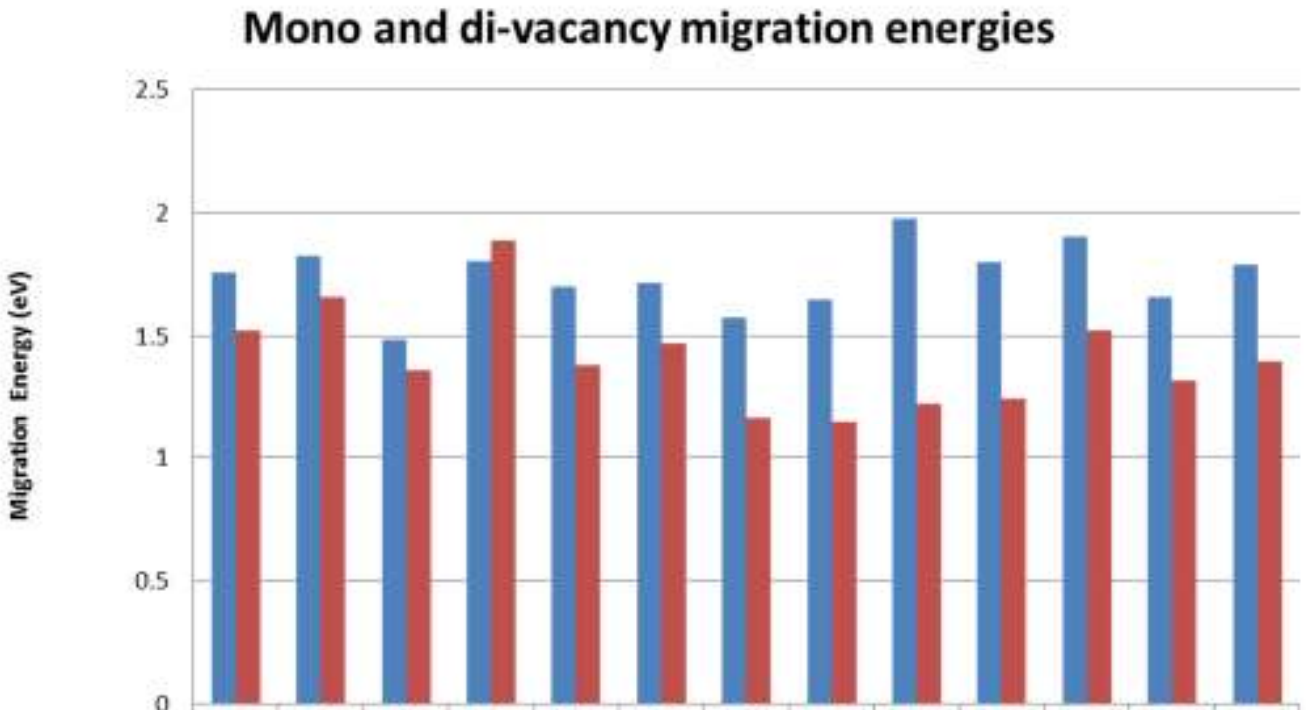

	1v1x1'	2v1x2 I	2v1x2 F	2v1x3 I	2v1x3 F	2v1x5 I	2v1x5 F	2v2x4 I	2v2x4 F	2v3x4 I	2v3x4 F	2v5x4 I	2v5x4 F
DFT	1.7564	1.8253	1.4904	1.8076	1.7005	1.7173	1.5753	1.6518	1.9798	1.8029	1.9031	1.6574	1.7925
Corrected AT	1.5244	1.6578	1.3622	1.8867	1.3854	1.4707	1.1686	1.1571	1.228	1.2485	1.5251	1.3198	1.3971

Tri-vacancy configuration changes

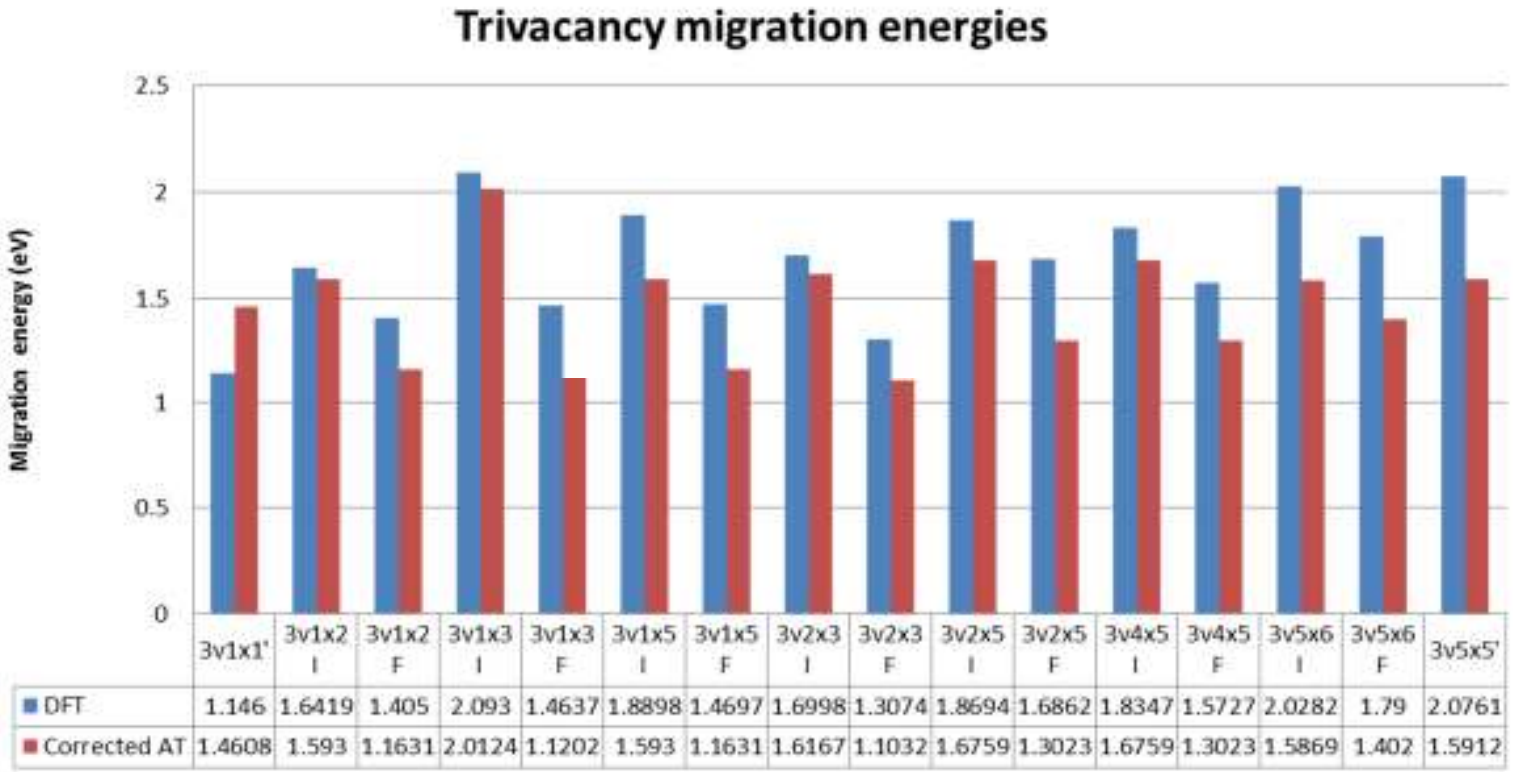

	3v1x1'	3v1x2 I	3v1x2 F	3v1x3 I	3v1x3 F	3v1x5 I	3v1x5 F	3v2x3 I	3v2x3 F	3v2x5 I	3v2x5 F	3v4x5 I	3v4x5 F	3v5x6 I	3v5x6 F	3v5x5'
DFT	1.146	1.6419	1.405	2.093	1.4637	1.8898	1.4697	1.6998	1.3074	1.8694	1.6862	1.8347	1.5727	2.0282	1.79	2.0761
Corrected AT	1.4608	1.593	1.1631	2.0124	1.1202	1.593	1.1631	1.6167	1.1032	1.6759	1.3023	1.6759	1.3023	1.5869	1.402	1.5912

3v1 configuration has the lowest migration energy (DFT: 1.15 eV, corrected AT: 1.46 eV).
This tri-vacancy can migrate without dissociation and changing its shape

Migration of tri-vacancy cluster without dissociation

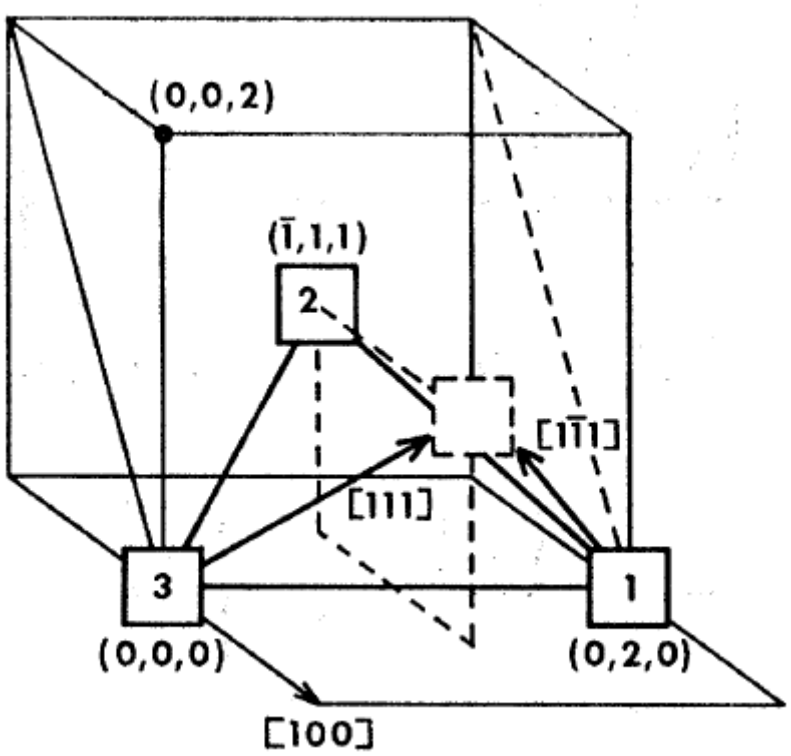

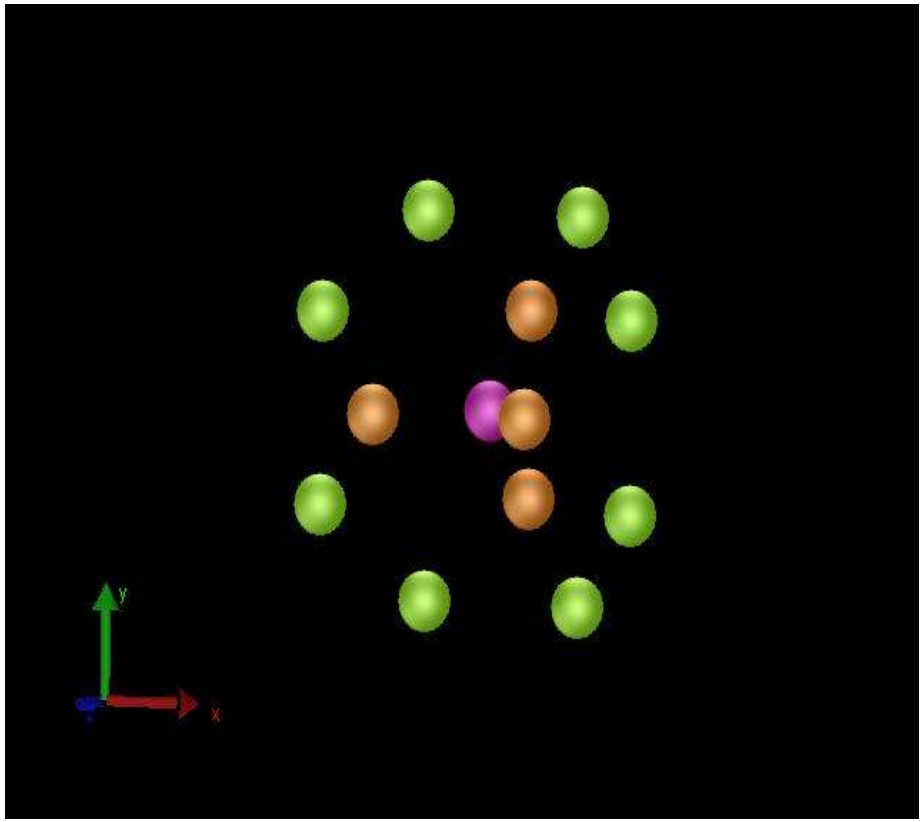

"Monkey" saddle point configuration of tri-vacancy cluster from DFT prediction

EUROfusion

WPMAT

Transferable of new W potentials into W-He system

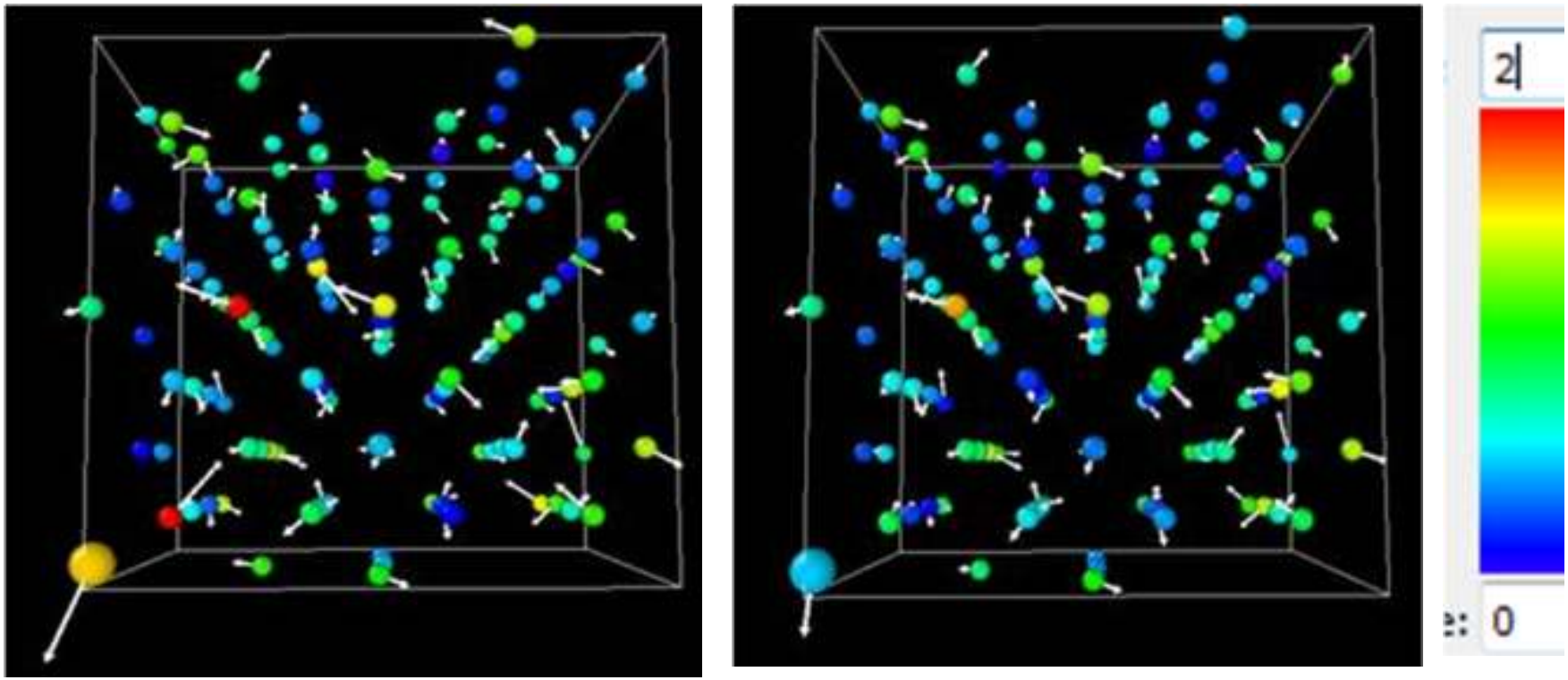

A. De Backer et al. (2015), unpublished

EUROfusion

WPMAT

Vacancy clusters: EAM-W vs. DFT

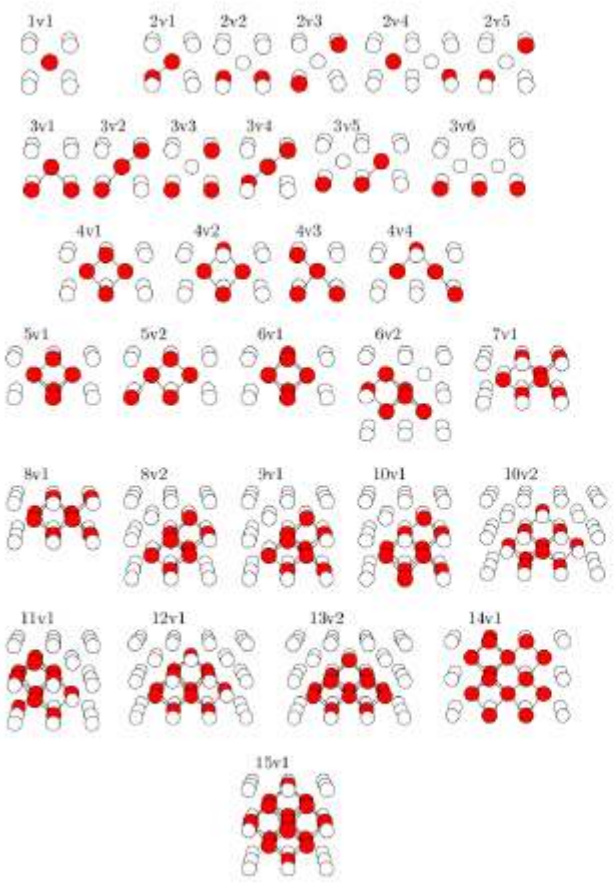

- EAM-W potential good for vacancy structures
  - Correct ordering of clusters
  - Relaxation volume
  - Formation energy

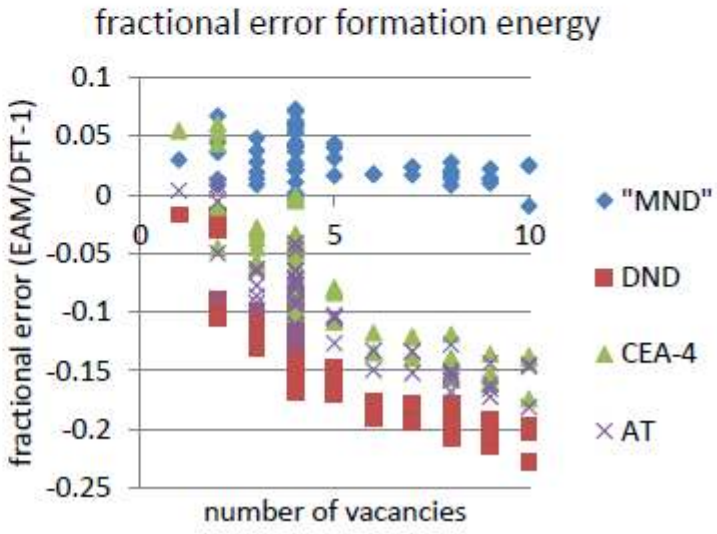

EUROfusion

WPMAT

KMC simulation of vacancy cluster dissociation

4-vacancy clusters

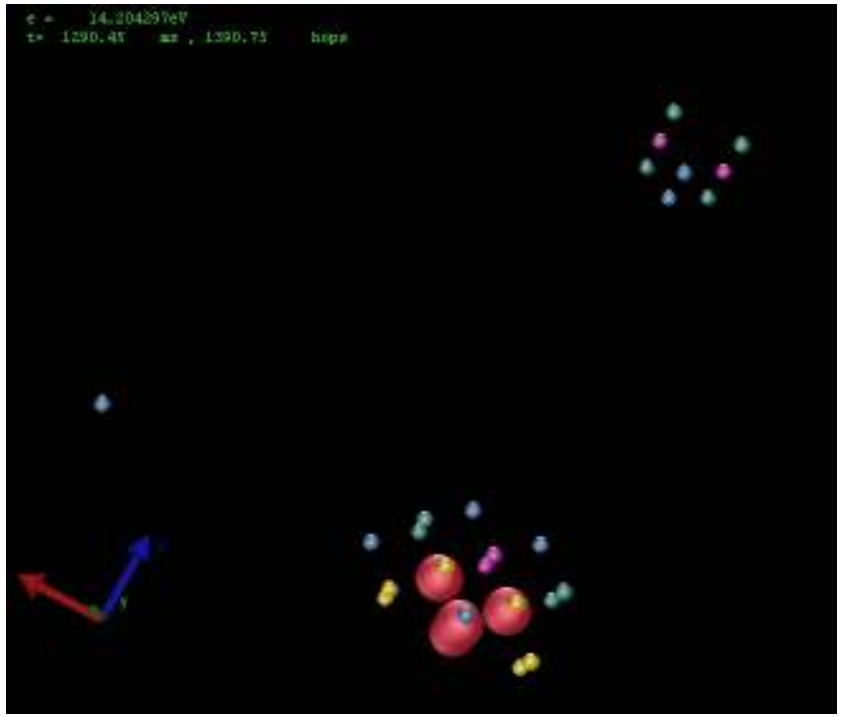

9-vacancy clusters

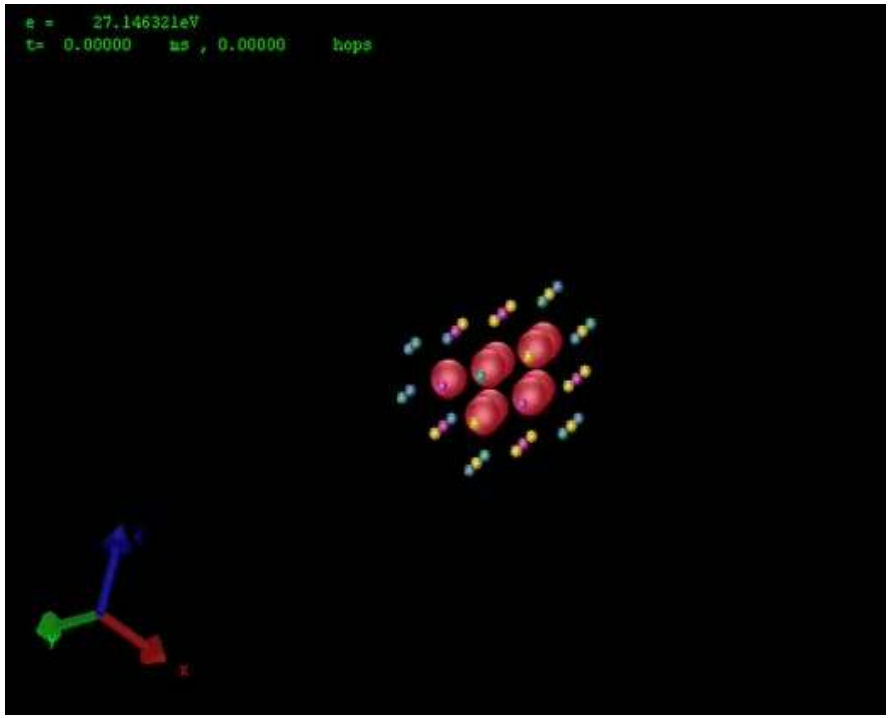

First frame is after 50 of kmc steps, corresponding to 240 first order moves, 42ms real time.
At frame 29, (10807 1st order moves, 2126ms) a vacancy splits off the cluster.
At frame 37 the monovac has found the cluster again, and at frame 45 it is off again.
Dissociation time is found from frame 29, the first time cluster does not immediately reform.

EUROfusion

WPMAT

Dissociation times and temperatures

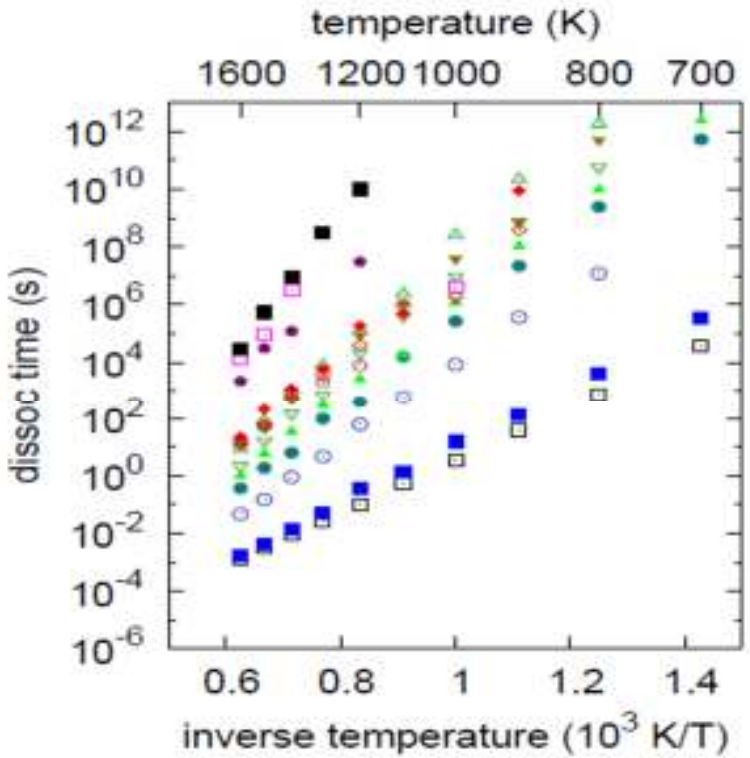

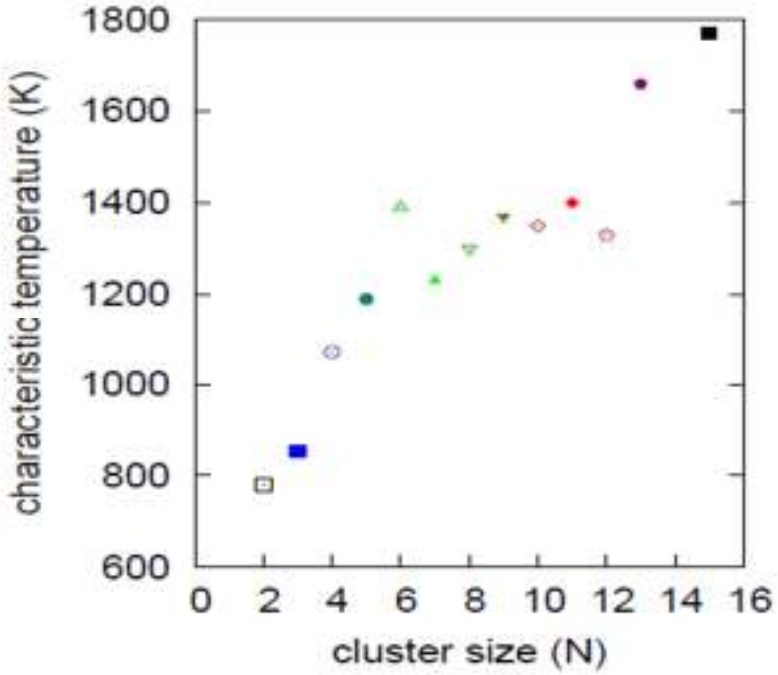

- Mean inverse dissociation rate for fixed cluster sizes and temperature
- Characteristic temperature at which dissociation rate = 1/s from Arrhenius plot

Effect of elastic relaxation

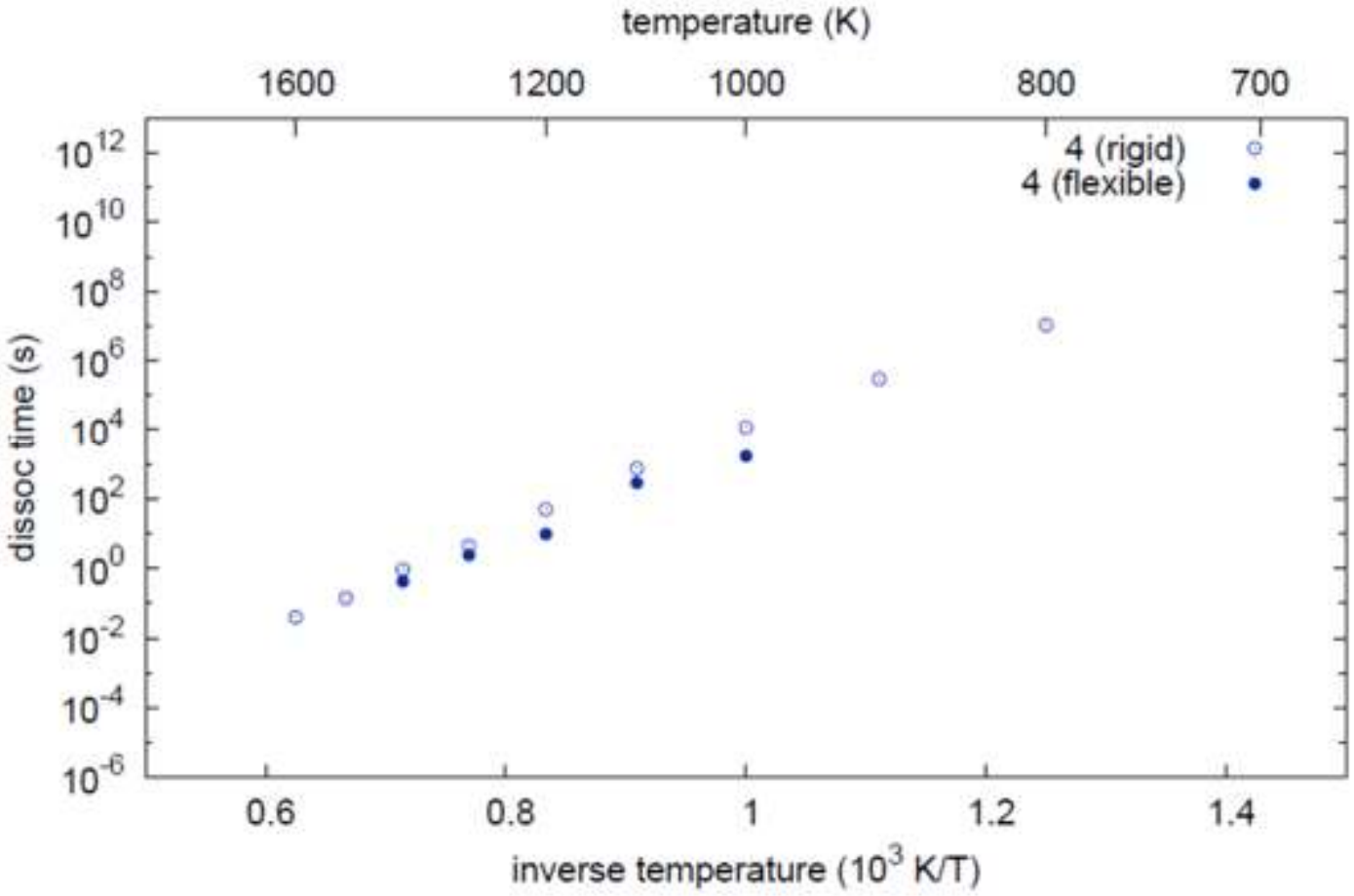

Ion-irradiation-induced clustering in W-Re, W-Re-Os

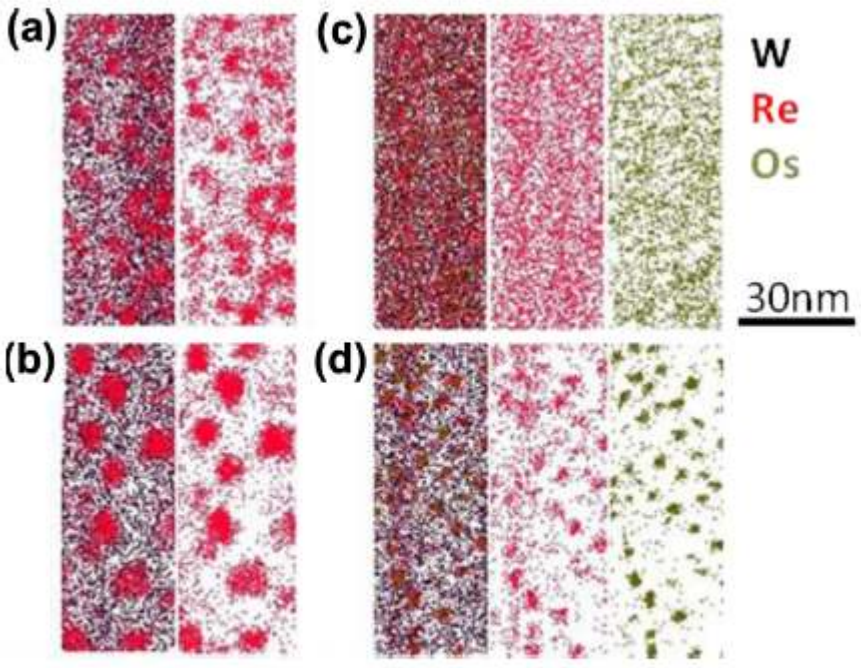

Fig. 2. 4 nm thick sections from atom maps showing species distribution following W–ion irradiation in: (a) W–2Re at 573 K, (b) W–2Re at 773 K, (c) W–1Re–1Os at 573 K and (d) W–1Re–Os at 773 K. W, Re and Os atoms are shown in black, red and green, respectively. (Color version of figure is available online.)

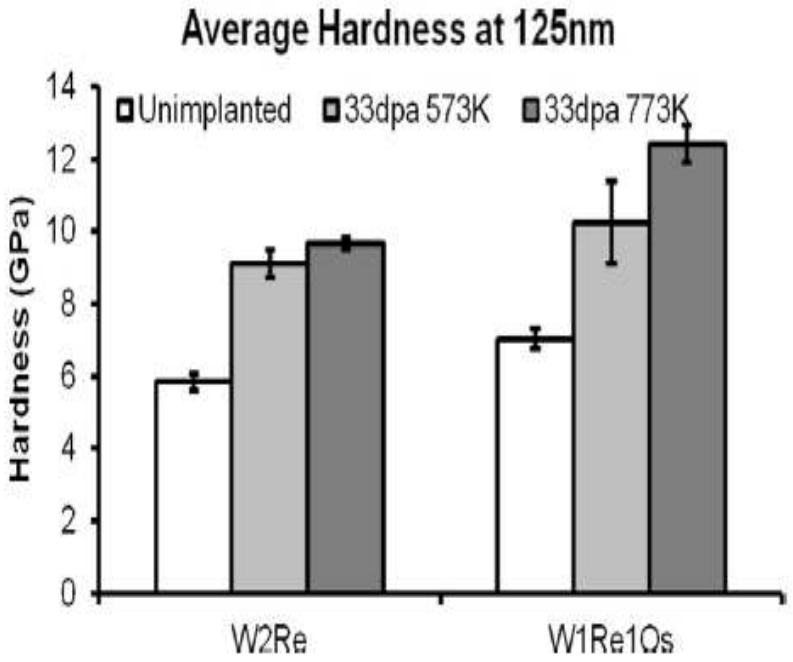

Fig. 5. Nanohardness measured at 125 nm indenter penetration depth for W–2Re and W–1Re–1Os at 573 and 773 K.

A. Xu et al., Acta Mat. 87 (2015) 121, APT and nano-indentation measurements of 33 dpa irradiation at 573K and 773K

Un-irradiated vs. irradiated W-Re and W-Re-Os alloys

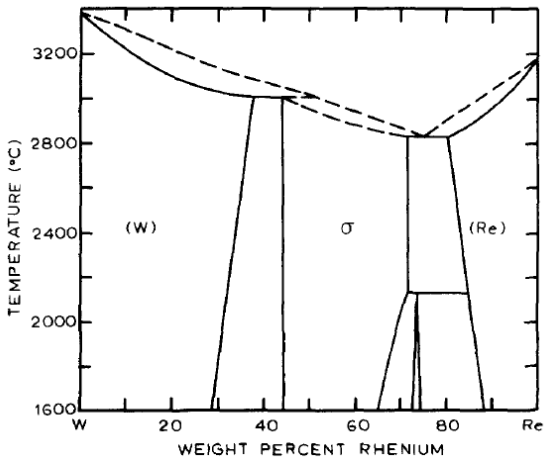

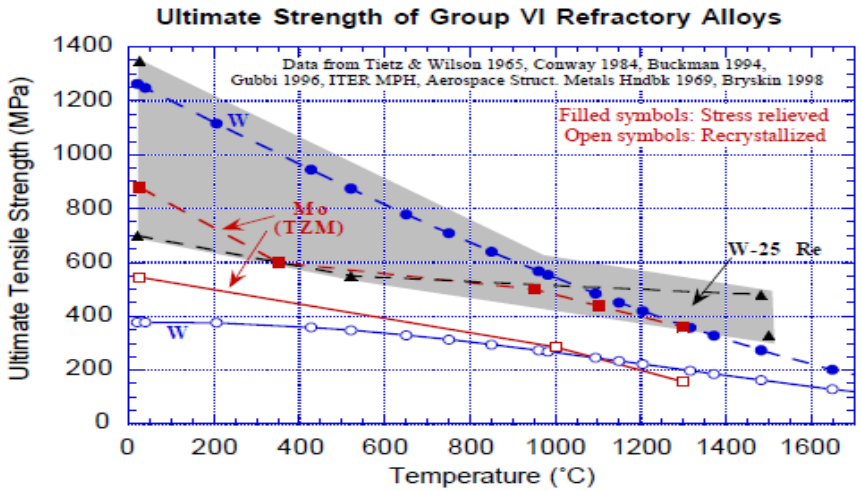

L. Romaner et al., PRL (2010): Effect of Re on dislocation core structure in W

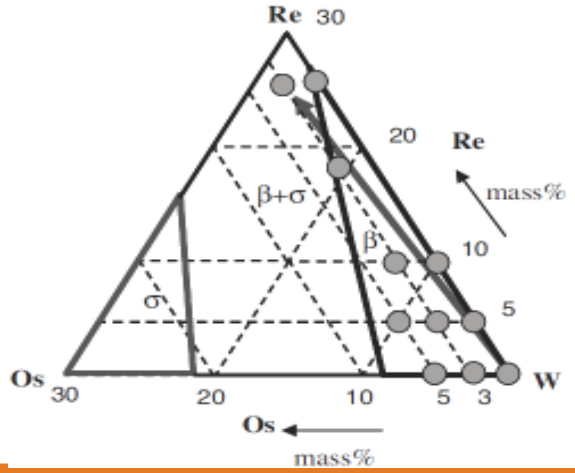

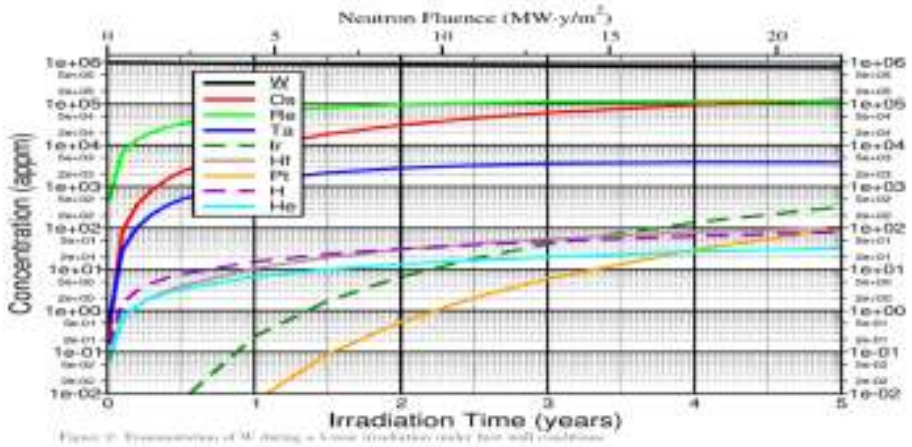

EUROfusion

WPMAT

Methods: Genetic algorithms to predict clustering from solute/point-defect interactions based on QM Hamiltonian

So far there are only DFT calculations of single point defect interaction with solute atom in W

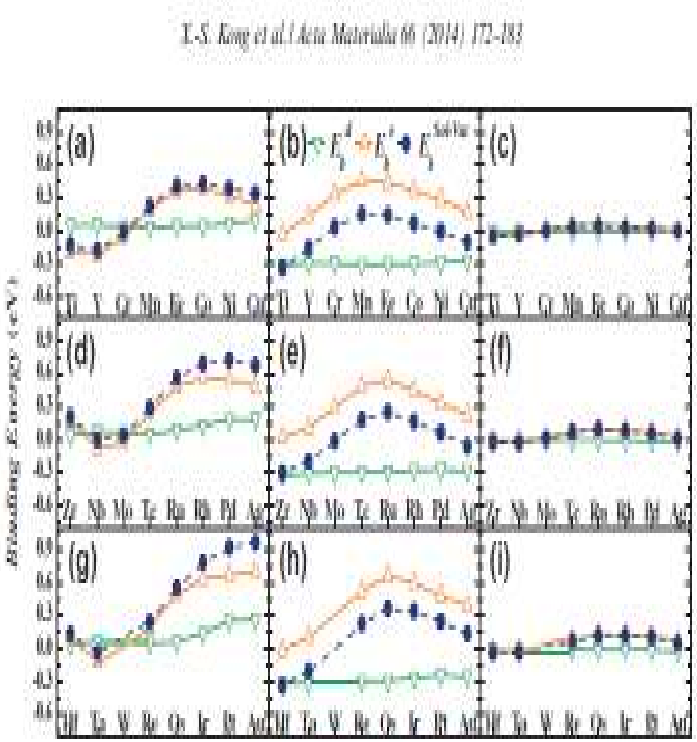

Fig. 4. Decomposition of the total solute-vacancy binding energy into distortion binding energy and electronic binding energy for the first to third nearest-neighbor relative positions (1nn: (a), (d), (g); 2nn: (b), (e), (h); 3nn: (c), (f), (i)).

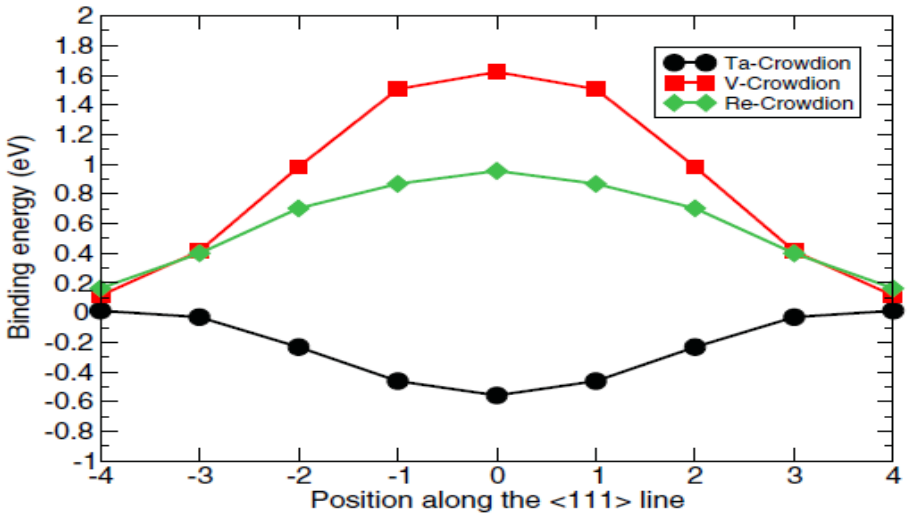

FIG. 14. (Color online) Binding energy of a crowdion interacting with substitutional Ta, V, and Re atoms in bcc-W lattice.

M. Muzyk, DNM, K. Kurzydlowski,
N. Baluc, S.L. Dudarev, PRB, 84 (2011) 041115;
T. Suzudo et.al., MSMSE, 22 (2014) 075006

Methods: A complex interatomic interaction from cluster expansion formalism for multi-component alloys including vacancies

$$\Delta H_{CE}(\vec{\sigma}) = \sum_{\omega} m_{\omega} J_{\omega} \langle \Gamma_{\omega'}(\vec{\sigma}) \rangle_{\omega},$$

J_ω are the **effective cluster interactions**
$\langle \Gamma_\omega(\vec{\sigma}) \rangle$ are the average **cluster functions**.

Binary: $\Gamma_\omega(\vec{\sigma}) = \sigma_1 \sigma_2 \ldots \sigma_{|\omega|}$

M component: $\Gamma_\omega(\vec{\sigma}) = \gamma_{1,M}(\sigma_1)\gamma_{2,M}(\sigma_2) \ldots \gamma_{|\omega|,M}(\sigma_{|\omega|})$

$$\begin{aligned}
\Delta H_{\mathrm{CE}}(\vec{\sigma}) = {} & J_1^{(0)} + J_1^{(1)}(1 - 3c_A) + J_1^{(2)}\frac{\sqrt{3}}{2}(c_C - c_B) + \sum_n^{\text{pairs}} \Big[\frac{1}{4} m_{2,n}^{(11)} J_{2,n}^{(11)} (1 + 3y_n^{AA} - 6y_n^{AB} - 6y_n^{AC}) \\
& + \frac{\sqrt{3}}{4} m_{2,n}^{(12)} J_{2,n}^{(12)} (-y_n^{BB} + y_n^{CC} + 2y_n^{AB} - 2y_n^{AC}) + \frac{3}{4} m_{2,n}^{(22)} J_{2,n}^{(22)} (y_n^{BB} + y_n^{CC} - 2y_n^{BC}) \Big] \\
& + \sum_n^{\text{triples}} \Big[\frac{1}{8} m_{3,n}^{(111)} J_{3,n}^{(111)} (-8y_n^{AAA} + 12y_n^{AAB} + 12y_n^{AAC} - 6y_n^{ABB} - 6y_n^{ABC} - 6y_n^{ACC} + y_n^{BBB} \\
& + 3y_n^{BBC} + 3y_n^{BCC} + y_n^{CCC}) + \frac{\sqrt{3}}{8} (m_{3,n}^{(112)} J_{3,n}^{(112)} + m_{3,n}^{(121)} J_{3,n}^{(121)} + m_{3,n}^{(211)} J_{3,n}^{(211)}) (-4y_n^{AAB} + 4y_n^{AAC} \\
& + 4y_n^{ABB} - 4y_n^{ACC} - y_n^{BBB} - y_n^{BBC} + y_n^{BCC} + y_n^{CCC}) + \frac{3}{8} (m_{3,n}^{(122)} J_{3,n}^{(122)} + m_{3,n}^{(212)} J_{3,n}^{(212)} + m_{3,n}^{(221)} J_{3,n}^{(221)}) (-2y_n^{ABB} \\
& + 2y_n^{ABC} - 2y_n^{ACC} + y_n^{BBB} - y_n^{BBC} - y_n^{BCC} + y_n^{CCC}) + \frac{3\sqrt{3}}{8} m_{3,n}^{(222)} J_{3,n}^{(222)} (-y_n^{BBB} + 3y_n^{BBC} - 3y_n^{BCC} + y_n^{CCC}) \Big] \\
& + \sum_n^{\text{multibody}} \cdots . \qquad \text{(A3)}
\end{aligned}$$

Fe-Cr-Ni: J.S. Wrobel, DNM, MY. Lavrentiev, M.Muzyk, S.L. Dudarev, PRB 91, (2015) 024108 (31)

EUROfusion

WPMAT

Application for W-Re-vacancy systems

- DFT data base for W-vac systems as discussed
- DFT data base for bcc W-Re
- Focusing on new Re-vac (clusters, voids) data base in bcc-W

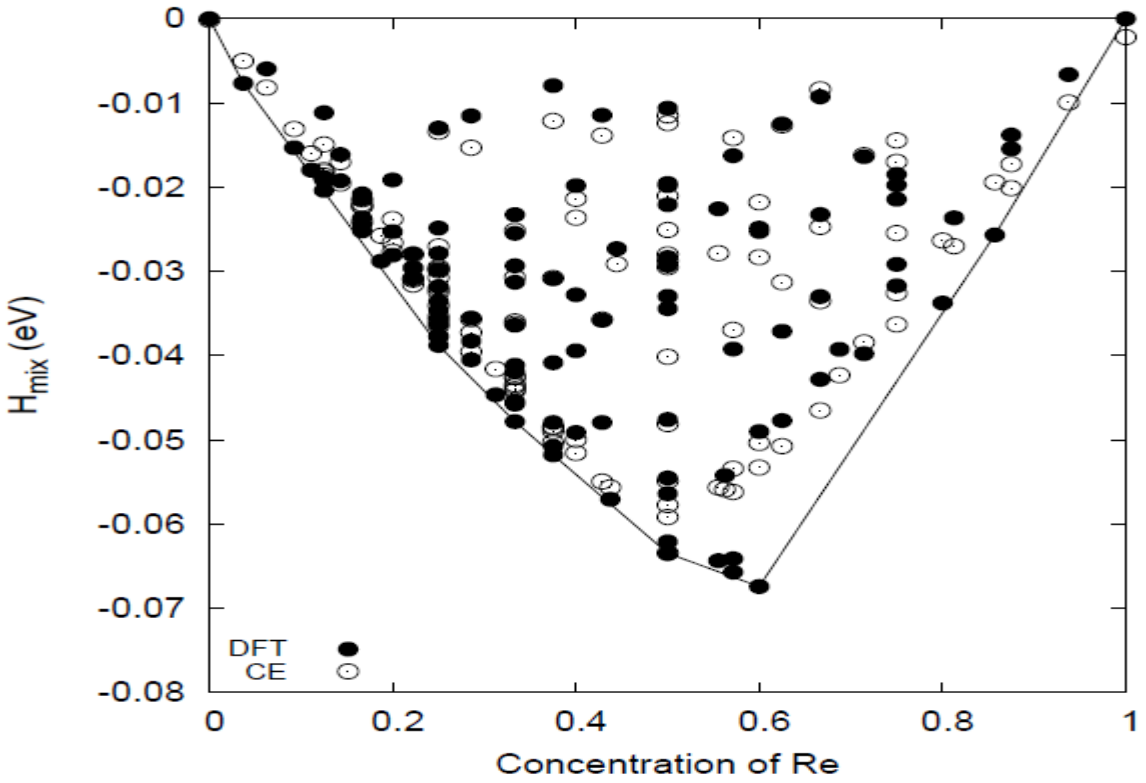

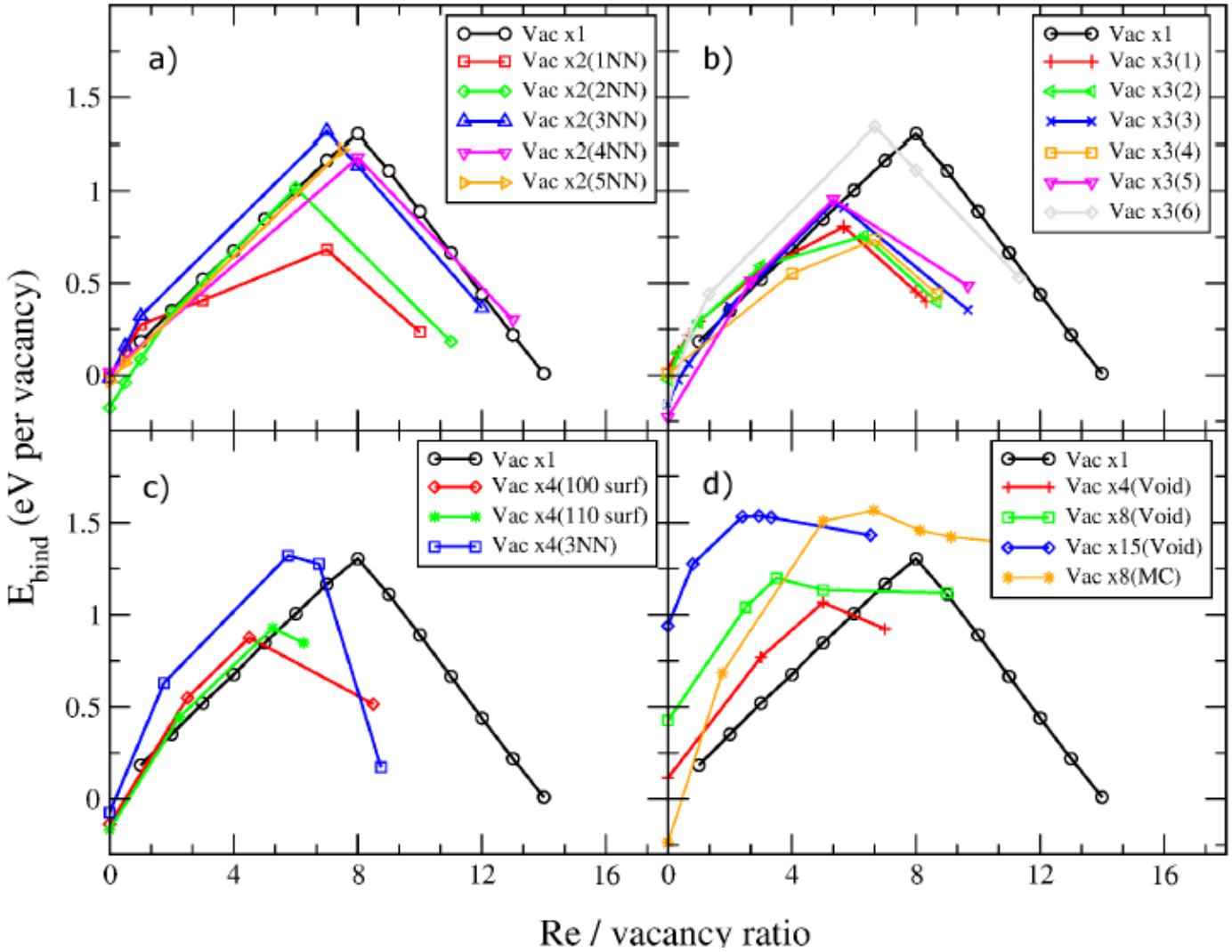
a)
Vac x1
Vac x2(1NN)
Vac x2(2NN)
Vac x2(3NN)
Vac x2(4NN)
Vac x2(5NN)
b)
Vac x1
Vac x3(1)
Vac x3(2)
Vac x3(3)
Vac x3(4)
Vac x3(5)
Vac x3(6)
c)
Vac x1
Vac x4(100 surf)
Vac x4(110 surf)
Vac x4(3NN)
d)
Vac x1
Vac x4(Void)
Vac x8(Void)
Vac x15(Void)
Vac x8(MC)
E_bind (eV per vacancy)
Re / vacancy ratio
0
0.5
1
1.5
0
4
8
12
16

EUROfusion

WPMAT

W-Re-vac: Effective cluster interactions

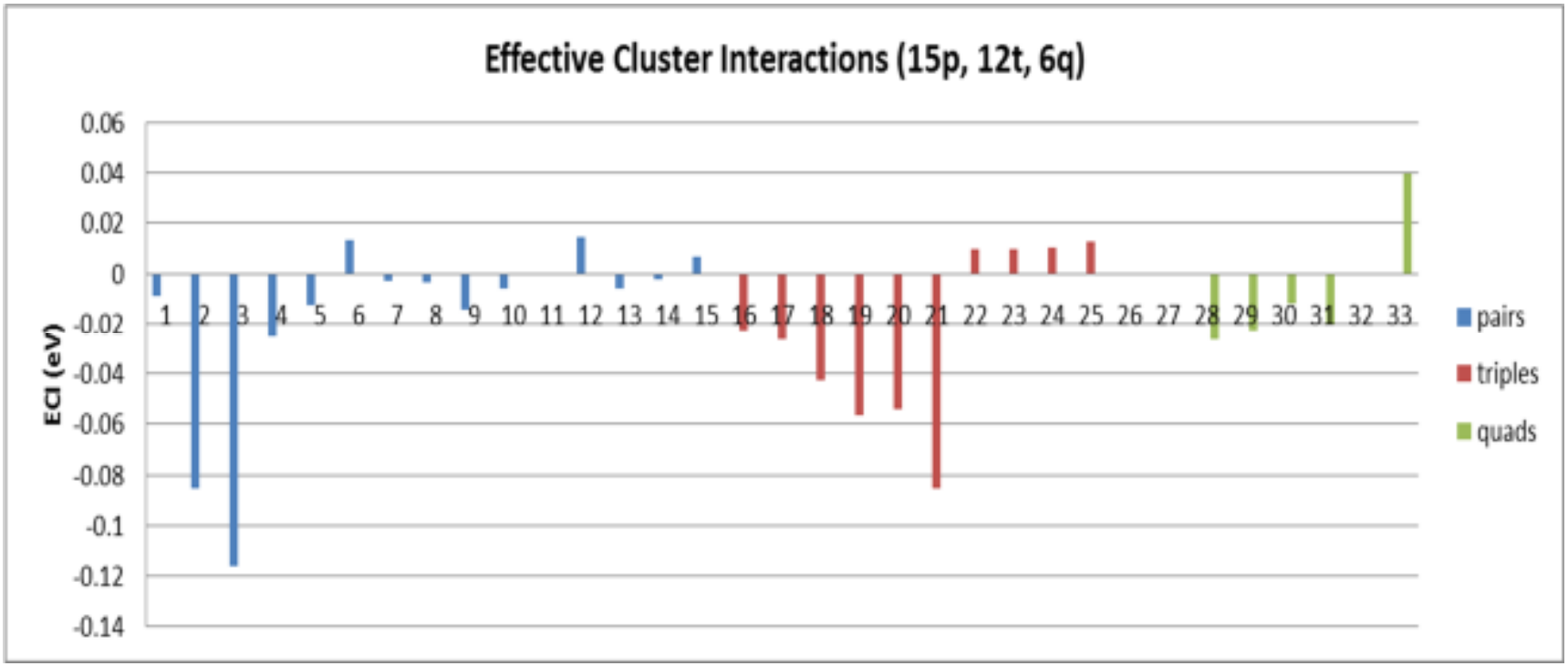

- More than 300 DFT energy configurations have been used
- Mapping into CE Hamiltonian gives a very good cross-validation value of 5.3 meV
- Pair and triple clusters are dominant

TABLE I. Monte Carlo results as a function of Re and vacancy concentration for alloys quenched down from high temperatures. MC simulations were performed starting from 2500 K. The alloys were cooled down with the temperature step of 100 K to the temperature of 100 K with 3000 MC steps per atom at the thermalization and accumulation stages.

	1% at. Re	2% at. Re	5% at. Re	10% at. Re
0.05% at. Vac	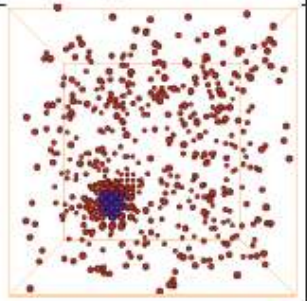	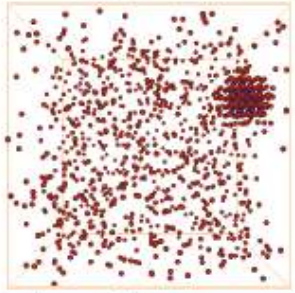	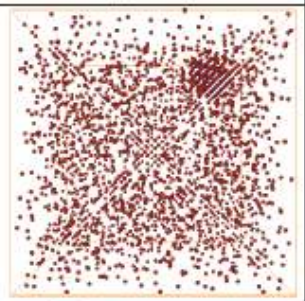	
0.1% at. Vac	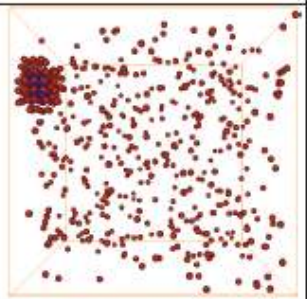	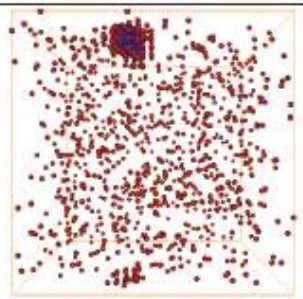	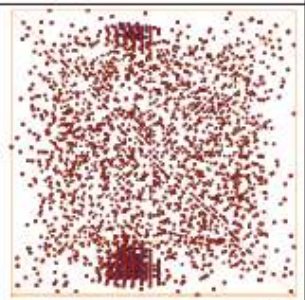	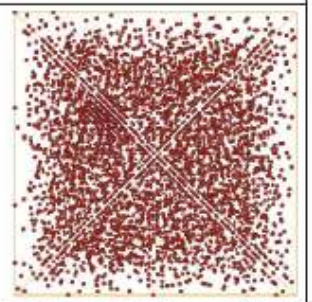
0.2% at. Vac	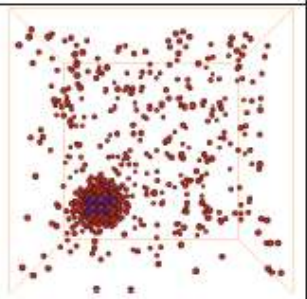	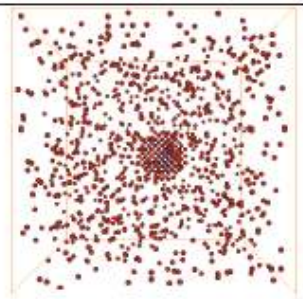	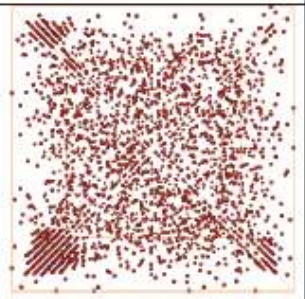	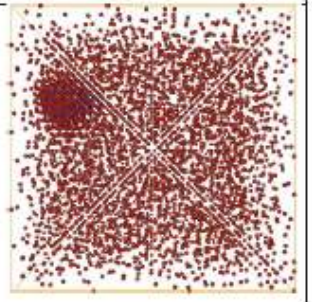

Results at T=2500K: dissociation of Re-vac clusters

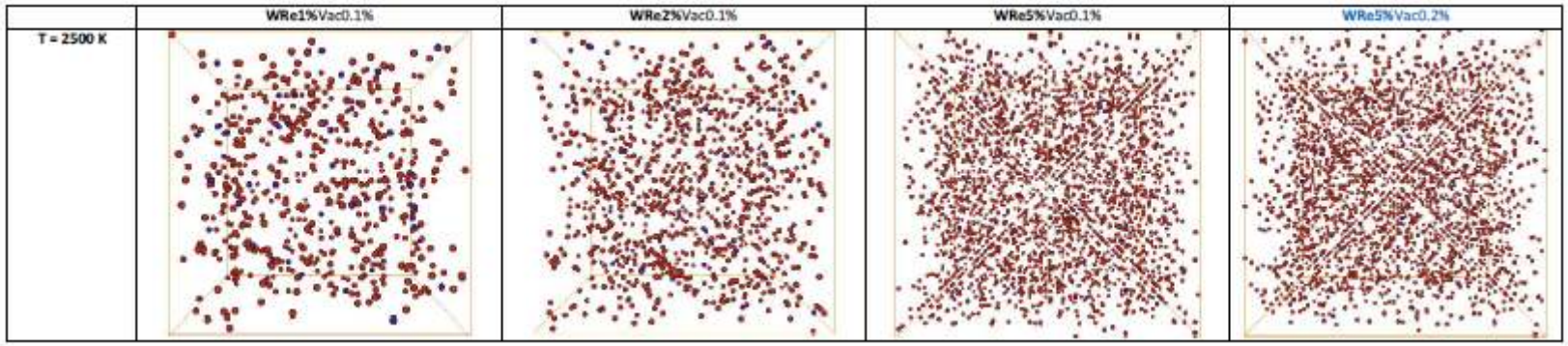

$$S_{\mathrm{conf}}(T) = \int_0^T \frac{C_{\mathrm{conf}}(T')}{T'} dT', \qquad (25)$$

where the configurational contribution to the specific heat C_{conf} is related to fluctuations of enthalpy of mixing at a given temperature [48,103] through

$$C_{\mathrm{conf}}(T) = \frac{\langle H_{\mathrm{mix}}(T)^2 \rangle - \langle H_{\mathrm{mix}}(T) \rangle^2}{T^2}, \qquad (26)$$

where $\langle H_{\mathrm{mix}}(T) \rangle$ and $\langle H_{\mathrm{mix}}(T)^2 \rangle$ are the mean and mean square average enthalpies of mixing, respectively, computed by averaging over all the MC steps at the accumulation stage for a given temperature.

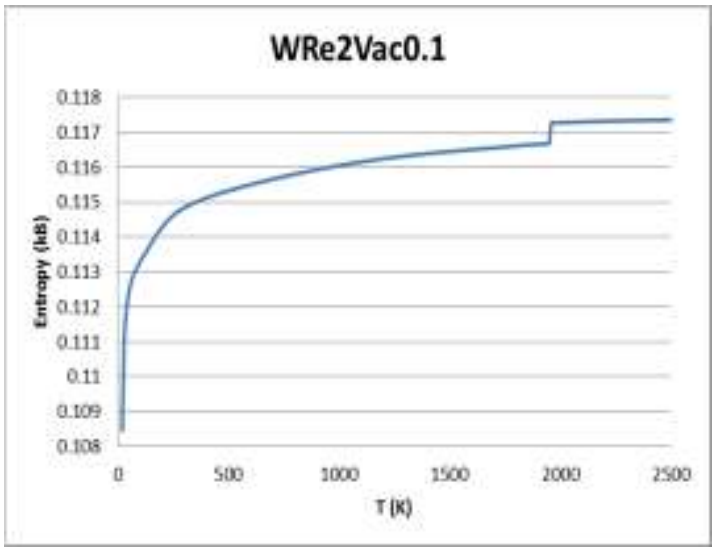

MC simulations vs. APT

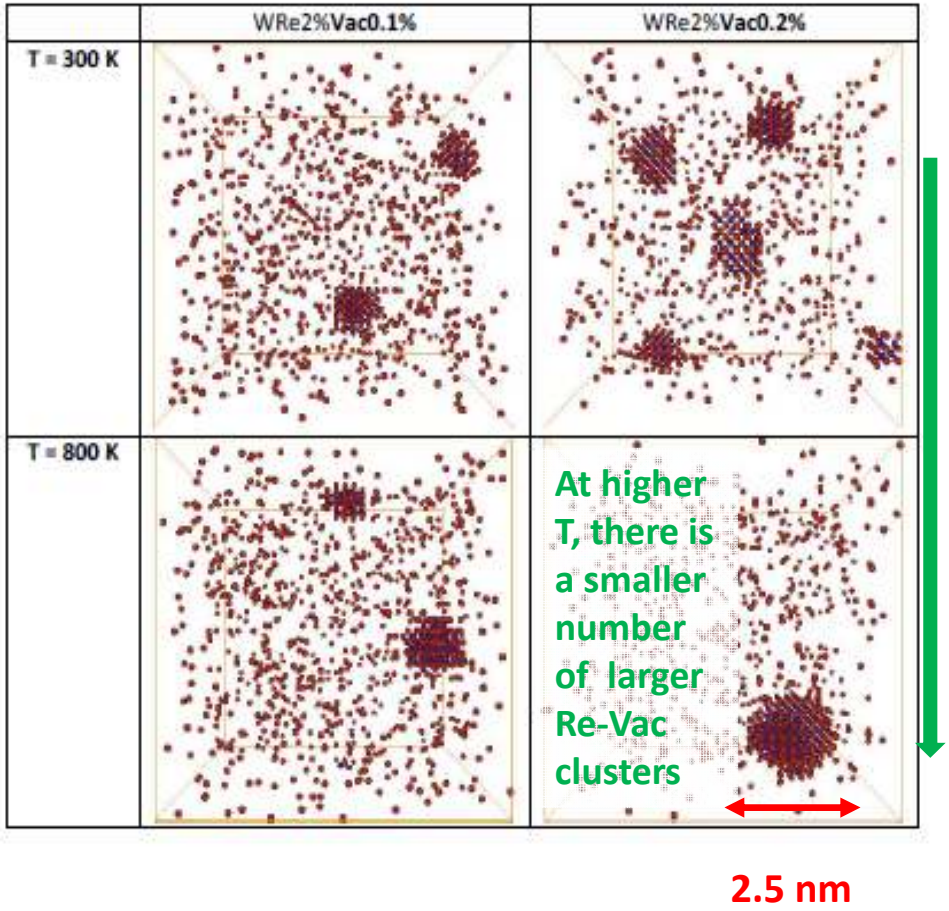

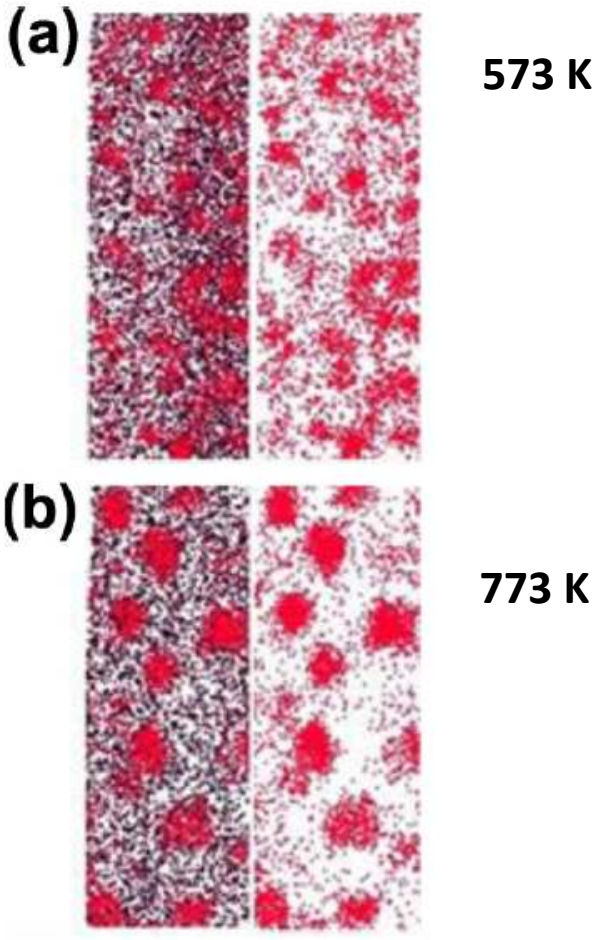

Re-Vac clusters from atomic-level analysis

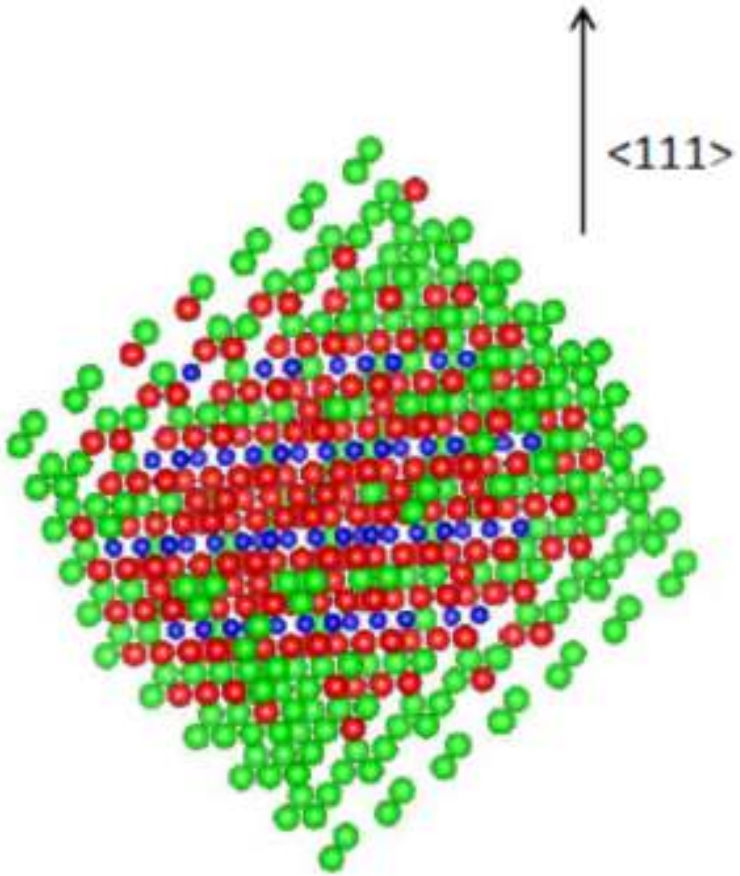

$$\Delta H_{\mathrm{CE}}(\vec{\sigma}) = J_1^{(0)} + J_1^{(1)}(1-3c_A) + J_1^{(2)}\frac{\sqrt{3}}{2}(c_C - c_B) - 4\sum_n^{\text{pairs}}\left(V_n^{AB}y_n^{AB} + V_n^{AC}y_n^{AC} + V_n^{BC}y_n^{BC}\right) + \sum_n^{\text{multibody}}\cdots, \quad (19)$$

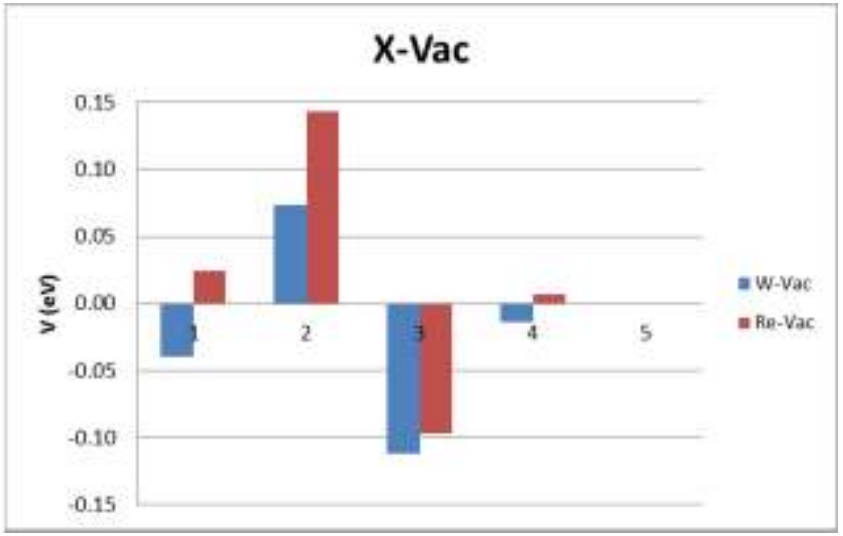

Conclusions

WPMAT

- For the stage 1, DFT prediction of recovery of SIA & vacancy recombination is in good agreement with experimental data (U low)
- DFT prediction of He trapping noble-gas impurities is also in excellent agreement with the TDS measurements. U remains for trapping of He clusters
- DFT allows to evaluate U from lattice swelling and modulus changes
- Surface-corrected DFT and inter-atomic potential produce a new insight for vacancy nano-cluster treatments in Stage IV. Systematic KMC prediction of characteristic temperature of nano-cluster vacancy dissociation corresponds with the temperature range of SIA dislocation loop loos. U can be evaluated from hierarchy of multi-scale modelling
- Hybrid DFT/CE/MC method has been generated for alloy with for W-Re-vacancy systems in order to explain experimental observation of anomalous Re-cluster precipitation under self-ion irradiation in W alloys. It opens a way to evaluate U for driven multi-component alloys